Title

Global Simulations of Phase State and Equilibration Time Scales of Secondary Organic Aerosols with GEOS-Chem.

Permalink

https://escholarship.org/uc/item/72v4w658

Journal

ACS Earth and Space Chemistry, 9(2)

ISSN

2472-3452

Authors

Luu, Regina
Schervish, Meredith
June, Nicole
et al.

Publication Date

2025-02-20

DOI

10.1021/acsearthspacechem.4c00281

ACS EARTH AND SPACE CHEMISTRY
Open Access

http://pubs.acs.org/journal/aesccq
Article

Global Simulations of Phase State and Equilibration Time Scales of Secondary Organic Aerosols with GEOS-Chem

Published as part of ACS Earth and Space Chemistry special issue "Hartmut Herrmann Festschrift".

Regina Luu, Meredith Schervish, Nicole A. June, Samuel E. O'Donnell, Shantanu H. Jathar, Jeffrey R. Pierce, and Manabu Shiraiwa*

Cite This: *ACS Earth Space Chem.* 2025, 9, 288−302

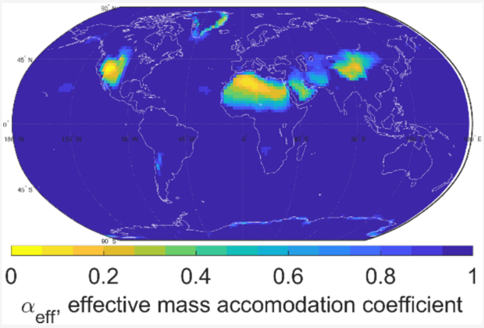

ABSTRACT: The phase state of secondary organic aerosols (SOA) can range from liquid through amorphous semisolid to glassy solid, which is important to consider as it influences various multiphase processes including SOA formation and partitioning, multiphase chemistry, and cloud activation. In this study, we simulate the glass transition temperature and viscosity of SOA over the globe using the global chemical transport model, GEOS-Chem. The simulated spatial distributions show that SOA at the surface exist as liquid over equatorial regions and oceans, semisolid in the midlatitude continental regions, and glassy solid over lands with low relative humidity. The predicted SOA viscosities are mostly consistent with the available measurements. In the free troposphere, SOA particles are mostly predicted to be semisolid at 850 hPa and glassy solid at 500 hPa, except over tropical regions including Amazonia, where SOA are predicted to be low viscous. Phase state also exhibits seasonal variation with a higher frequency of semisolid and solid particles in winter compared to warmer seasons. We calculate equilibration time scales of SOA partitioning (τ_{eq}) and effective mass accommodation coefficient (α_{eff}), indicating that τ_{eq} is shorter than the chemical time step of GEOS-Chem of 20 min and α_{eff} is close to unity for most locations at the surface level, supporting the application of equilibrium SOA partitioning. However, τ_{eq} is prolonged and α_{eff} is lowered over drylands and most regions in the upper troposphere, suggesting that kinetically limited growth would need to be considered for these regions in future large-scale model studies.

KEYWORDS: *viscosity, mass accommodation coefficient, SOA partitioning, kinetic model, volatility, chemical transport model*

■ INTRODUCTION

Aerosol particles regulate Earth's radiative balance by directly scattering or absorbing solar radiation and indirectly impacting cloud formation by serving as nuclei for cloud droplets and ice crystals.[1] Secondary organic aerosols (SOA) comprise approximately 30−70% of the submicron particulate mass in the lower troposphere, playing a major role in aerosol effects on climate, air quality and public health.[2−4] SOA are mainly formed via oxidation of volatile organic compounds and subsequent gas-particle partitioning.[5] SOA formation and growth are often modeled with absorptive equilibrium partitioning of semivolatile organic compounds, assuming implicitly that SOA particles adopt a low viscous liquid state.[6]

There is mounting evidence that SOA can exist in amorphous semisolid and glassy solid phase states depending on chemical composition and environmental conditions such as temperature and relative humidity (RH).[7,8] Both ambient- and laboratory-generated SOA particles have been observed to bounce under low RH conditions, indicative of nonliquid states.[9,10] Several techniques were developed to directly measure phase state and viscosity of SOA,[8] demonstrating that SOA adopt glassy and semisolid states especially under low RH and temperature.[11,12] Adopting a highly viscous phase state can impact a number of multiphase aerosol processes.[13] It causes kinetic limitations in partitioning of semivolatile species between the gas- and particle phases by prolonging the equilibration time scale of SOA partitioning.[14,15] Kinetically limited particle growth alters the evolution of particle size distributions in comparison to quasi-equilibrium growth behavior.[16−19] Chamber experiments probing particle−particle mixing time scales of SOA particles have observed kinetic limitations at low RH but not at moderate and high RH,[20−23] as time scales for particle−particle mixing are affected by a complex interplay among volatility, diffusion limitations, and nonideal miscibility.[24] The occurrence of glassy SOA in the

Received: September 24, 2024
Revised: February 3, 2025
Accepted: February 4, 2025
Published: February 11, 2025

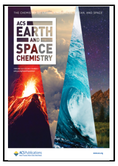

https://doi.org/10.1021/acsearthspacechem.4c00281

free troposphere may impact activation pathways of ice nuclei (IN) and cloud condensation nuclei (CCN).[25−28] Slow diffusion of oxidants and organic molecules can slow down heterogeneous and multiphase reactions,[29−34] facilitating long-range transport of toxic compounds that may be embedded in highly viscous particles.[3,35] Despite the relevance and importance of phase state on various atmospheric processes, most large-scale air quality and climate models do not resolve the SOA phase state and its effect on gas-particle partitioning, multiphase chemistry, and cloud activation.

Particle-phase state can be inferred from glass transition temperature (T_g), which can be converted into particle viscosity and consequently, bulk diffusivity using the Stokes−Einstein equation.[7,36,37] Several parametrizations have been developed to predict T_g as a function of molar mass, atomic O:C, and elemental composition.[36,38] A recently developed parametrization of T_g is based on O:C and volatility (C^0),[39] which can be directly incorporated into the two-dimensional volatility basis set (2D-VBS) framework.[40] This methodology has been applied to simulate the SOA phase state in chemical transport models for the regional and global scales.[38,41−44] At the global scale, SOA is predicted to be mostly glassy solid in the free troposphere.[38] Using a regional model CMAQ, Li et al. (2021) showed that SOA over the western US has higher T_g and viscosity compared to over the eastern US, corresponding to geospatial surface-level RH patterns.[43] Schmedding et al. (2020) found that organic-rich shells in phase-separated SOA particles are typically semisolid over the western US. Zhang et al. (2024) found that northwestern China tends to have highly viscous SOA particles with southern China exhibiting the highest frequency of particles predicted to be in the liquid state during summer.[45] In the Amazon rainforest, a liquid phase state is predicted to dominate with some occurrences of semisolid state at low altitude.[41]

Despite the importance of the SOA phase state and several CTM studies on spatial variability, there still lacks an analysis of the seasonality accompanying viscosity and bulk diffusivity changes modeled in the global scale. Heterogeneity in equilibration time scales of SOA partitioning (τ_{eq}) at a global scale has not been investigated, even though they are critical to validate an employed assumption of instantaneous SOA partitioning. In this study, we simulate the global distribution and seasonal variations of the SOA phase state and conduct sensitivity studies to analyze the dominating molecular parameters including hygroscopicity and the O:C. Then, we calculated τ_{eq} and the effective mass accommodation coefficient to evaluate the validity of instantaneous partitioning assumptions made in CTMs.

■ METHODS

GEOS-Chem Model Description. We used the global chemical transport model, GEOS-Chem (ver. 14.1.1) to simulate organic aerosols in the troposphere.[46−48] The model system was applied to simulate the atmospheric composition for the year 2020 with a horizontal grid resolution of 2° × 2.5° and 72 vertical layers extending to about 80 km altitude (0.1 hPa). The model was spun up with a preliminary 11-month simulation, after which the following 12-month outputs were recorded and analyzed. The model was driven by the Modern-Era Retrospective Analysis for Research and Applications (MERRA) v2 meteorological data products to provide 3-h instantaneous ambient temperatures and 3-h averaged RH.[49] The transport time step is 10 min, while the chemical time step is 20 min. Global emissions inventories of considered SOA precursors were supplied through the default configuration of the Harmonized Emissions Component (HEMCO), which is directly coupled to GEOS-Chem.[50] Additional HEMCO emissions and extensions are listed in Table S2. For anthropogenic emissions, we used the Community Emissions Data System (CEDS) v2.[51] For biogenic emissions, we used offline VOC emissions[52] computed from the Model of Emissions of Gases and Aerosols from Nature (MEGAN) v2.1.[53]

The full chemistry mechanism with the complex SOA with semivolatile POA (SVPOA) scheme option was applied. In the complex SOA scheme, all SOA components are treated with the volatility basis set (VBS) apart from isoprene SOA and organo-nitrate SOA, which are explicitly modeled through the respective aqueous-phase irreversible reactive uptake schemes.[54,55] Currently, this mechanism does not include aqueous-phase processing of SOA precursors (aside from isoprene SOA and organo-nitrate SOA) nor autoxidation for the formation of highly oxygenated organic molecules (HOMs), which have very low volatility and are expected to condense irreversibly onto particles.[56−58] The total mass loadings of relevant organic aerosols are composed of the oxidation products of monoterpenes and sesquiterpenes (TSOA), oxidation products of light aromatics and intermediate volatility organic compounds (IVOCs) (ASOA), isoprene epoxydiols (IEPOX)-derived SOA (SOAIE), aerosol-phase non-IEPOX product of isoprene hydroxy hydroperoxides (LVOCOA), and aerosol-phase glyoxal (SOAGX) species (Table S3). ASOA is treated by lumping oxidation products of light aromatics and IVOCs as they exhibit similar SOA yields,[59] and previous modeling and observational studies found their significant contributions in megacities.[60−62]

Additionally, in the complex scheme, oxygenated primary organic aerosols (OPOA) are formed from oxidation products of primary emitted organic gases (EPOA).[63] Previous studies have treated OPOA differently either as primary organic aerosol[63,64] or SOA.[65,66] In this study, we have chosen to omit OPOA from our main SOA phase state and equilibration time scale calculations, as only two volatility bins each are used to represent both EPOA and their oxidation products, OPOA,[64,67] which may not be sufficient constraints especially for phase state predictions.[68,69] Nevertheless, we conduct sensitivity simulations to evaluate the potential impacts of including OPOA in the SOA phase state. All SOA species were classified into volatility bins and separated into effective saturation mass concentrations $C^*(300\text{ K})$ (in μg m^{-3}) using the VBS approach.[70] As specified in Table S4, the TSOA volatility bins are $C^*(300\text{ K}) = 0.1$, 1, 10, and 100 μg m^{-3}, and the ASOA volatility bins are C^* (300 K) = 10^{-4}, 1, 10, and 100 μg m^{-3}.[71] The ASOA lowest volatility bin (C^* (300 K) = 10^{-4} μg m^{-3}) is represented in GEOS-Chem as a nonvolatile (under relevant atmospheric conditions) component of anthropogenic oxidation products.[64] In addition, TSOA and ASOA volatility bin definitions used here are based on SOA yield parametrizations from previous chamber experiments with details described in Pye et al.[59] To explore the impacts of such (extremely) low-volatility compounds (LVOC/ELVOC) on viscosity, we conduct sensitivity simulations by changing the lowest volatility bin of the TSOA species from 0.1 to 10^{-4} μg m^{-3} for T_g estimations. The ASOA O:C values were prescribed based on laboratory studies[72] and TSOA O:C was based on the oxygenation of C_{10} compounds in the atmosphere.[40] Since

LVOCOA and SOAGX were defined by a single surrogate compound, their chemical formulas, $C_5H_{14}O_5$ and $C_2H_2O_2$, were used for assigning the O/C and molar masses. T_g of SOAIE was prescribed based on available T_g measurements of IEPOX-derived SOA[73] rather than being estimated using the parametrizations by assigning O:C and C^0.

Glass Transition Temperature, Viscosity, and Bulk Diffusivity. We applied the following parametrization to estimate glass transition temperatures (T_g) of organic compounds in volatility bin as a function of C^0 and O:C.[39]

$$T_g = 289.10 - 16.50 \times \log_{10}(C^0) - 0.29 \times [[\log_{10}(C^0)]^2 + 3.23 \times \log_{10}(C^0)(\mathrm{O{:}\ C})] \tag{1}$$

C^0 is the pure compound saturation mass concentration at 298 K, and we assume that C^* is equal to C^0 with ideal mixing conditions (activity coefficient as unity). Molar mass was assigned for each volatility bin using the molecular corridor approach[38,74] and O:C was assigned based on previous work as specified in Table S2. T_g of dry SOA ($T_{g,org}$) is calculated as $T_{g,org} = \sum_i \omega_i T_{g,i}$ or the sum of the mass-weighted fractions of each bin i and its calculated $T_{g,i}$ using eq 2. ω_i is the mass fraction in each bin, which can be calculated by using VBS-outputted concentration in each volatility bin.

The Gordon−Taylor equation can be applied to estimate T_g of SOA particles that consist of organic and water mixtures.[7,38]

$$T_g(\omega_{org}) = \frac{(1-\omega_{org}) \times T_{g,w} + (1/k_{GT}) \times \omega_{org} T_{g,org}}{(1-\omega_{org}) + (1/k_{GT}) \times \omega_{org}} \tag{2}$$

The glass transition temperature of pure water ($T_{g,w}$) is 136 K and the Gordon−Taylor constant for organic-water mixtures (k_{GT}) is assumed to be 2.5.[7,28,38] ω_{org} is the organic mass fraction of SOA which is calculated as $\omega_{org} = m_{SOA}/(m_{SOA} + m_{H2O})$, where m_{SOA} is the mass concentration of SOA as outputted by the model and m_{H2O} is the mass concentration of water. From the MERRA-2 meteorological and the GEOS-Chem output, ambient RH and SOA mass concentrations are used to determine the mass concentration of water absorbed by SOA (m_w) as[75]

$$m_w = \frac{\kappa \rho_w m_{SOA}}{\rho_{SOA}((1/\mathrm{RH}) - 1)} \tag{3}$$

The effective hygroscopicity parameter (κ) for SOA is assumed to be 0.1 for the base case simulations,[75,76] which we varied in the range of 0.05−0.15 for sensitivity simulations. The density of water (ρ_w) and SOA particles (ρ_{SOA}) are assumed to be 1.0 and 1.4 g cm^{-3}, respectively.[77] The mass concentration of the SOA particles (m_{SOA}) is the sum of the mass concentrations of all SOA species.

In this work, we implicitly assume that SOA particles are either externally mixed with inorganic compounds such as sulfate and nitrate, similar to the current treatment in GEOS-Chem, or internally mixed with inorganics with phase separation of organic and inorganic compounds, as has been shown to occur under a wide range of RH.[78] In the latter case, our predicted viscosity represents the phase state of the organic phase, and resulting calculated equilibration time scales of SOA partitioning would be upper bound estimates. The limitation with this approach is that inorganic species, such as ammonium sulfate, ammonium nitrate, and sodium chloride, are not considered in determining the bulk phase state. If they are well-mixed, inorganic compounds may decrease viscosity by acting as a plasticizer, or they might enhance viscosity by forming a highly viscous gel.[79] A recent study has suggested that the presence of divalent cations complexed with organic material in marine aerosols may promote hydrogel formation resulting in a semisolid or solid state even at high RH.[80] These aspects are beyond the scope of this study but warrants future investigations by resolving phase separation, as has been done in a regional model study.[44]

The phase state of SOA is represented as T_g scaled over ambient temperatures (T_g/T) because the particle phase is determined by its T_g relative to ambient temperature. When $T_g/T \geq 1$, SOA particles adopt a glassy or amorphous solid state. When $T_g/T < 1$, SOA particles exist in semisolid or liquid states. The threshold between semisolid and liquid states depends on the so-called fragility parameter (D). In this study, we assume $D = 10$ based on our previous analysis,[36] resulting in the threshold of $T_g/T \sim 0.8$. SOA dynamic viscosity (η) is estimated with the modified Vogel−Fulcher−Tammann (VFT) equation.[81] As described in our previous studies,[36,38] the Vogel temperature, T_0 (K) and viscosity (Pa s) can be described using T_g and D as follows

$$T_0 = \frac{39.17 \times T_g(\omega_{org})}{D + 39.17} \tag{4}$$

$$\log(\eta) = -5 + 0.434 \times \frac{T_0 D}{T - T_0} \tag{5}$$

Fragility describes how a material's dynamics slow down as the surrounding temperature approaches the material's T_g. The viscosity can be converted into the bulk diffusion coefficient (D_b, cm^2 s^{-1}) using the fractional Stokes−Einstein equation

$$D_b = \frac{kT}{6\pi a \eta_c} \times \left(\frac{\eta_c}{\eta}\right)^{\xi} \tag{6}$$

where k is the Boltzmann constant, η_c is the crossover viscosity (1×10^{-3} Pa s),a is the hydrodynamic radius of a diffusing species (0.38 nm), and ξ is an empirical fit parameter determined to be 0.93 with these values based on Evoy et al.[82]

Using the derived D_b, the characteristic mixing time scales of bulk diffusion (τ_{mix}) within a single particle can be calculated as[29,83]

$$\tau_{mix} = \frac{d_p^2}{4\pi^2 D_b} \tag{7}$$

where d_p is particle diameter which is assumed to be 100 nm and τ_{mix} is the time scale for a diffusing molecule to mix within the particle.[14]

Equilibration Time Scale. The equilibration time scale of SOA partitioning (τ_{eq}) represents the *e*-folding time for semivolatile species to reach gas-particle equilibrium. τ_{eq} is determined through simulations using the kinetic multilayer model of gas-particle interactions in aerosols and clouds (KM-GAP) which has been described in detail previously.[14,84] A brief description and the specifics of the implementation for this work are addressed here, with additional information about used variables in Table S5. KM-GAP explicitly treats all steps of mass transport of semivolatile species diffusing from the gas phase into the particle phase.[84] The processes included are gas-phase diffusion, adsorption and desorption, surface-bulk exchange, and bulk diffusion. These processes occur across a number of layers: gas phase, sorption, near-surface

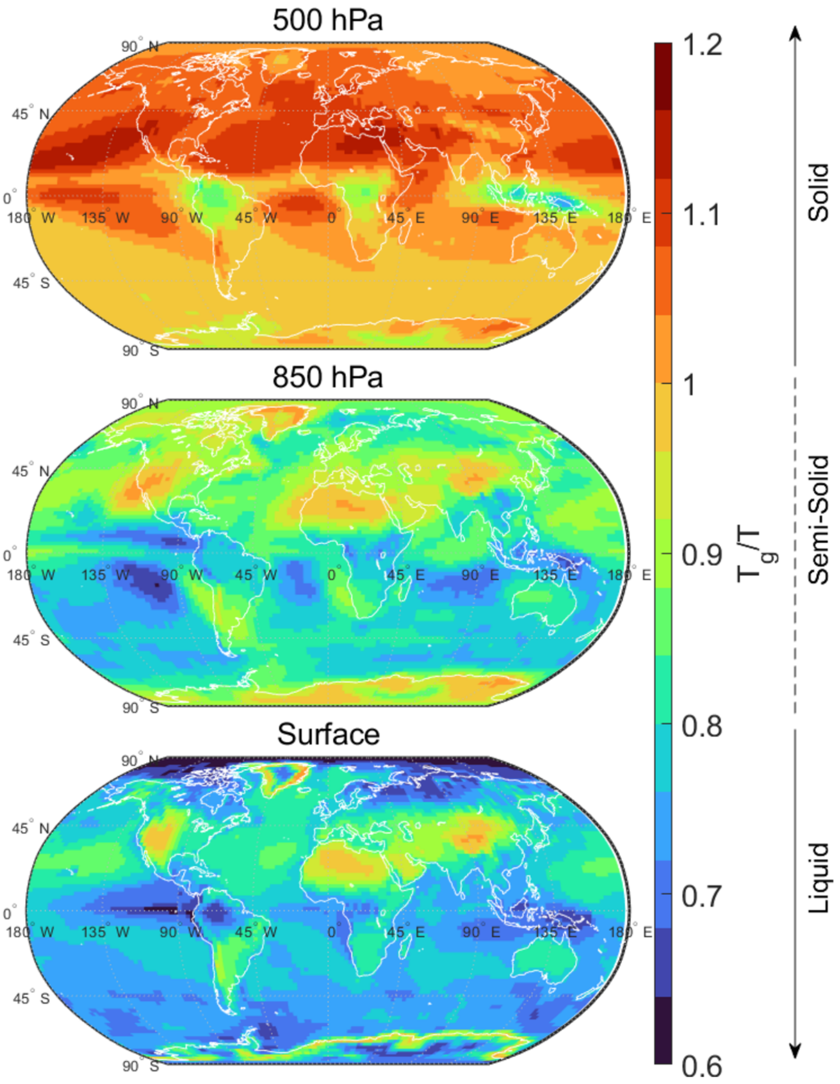

Figure 1. Predicted annual averages of glass transition temperature (T_g) scaled by ambient temperature (T) for SOA (T_g/T) at the surface level, 850 and 500 hPa, respectively, averaged for the year 2020. T_g/T is a measure of the phase state: $T_g/T \geq 1$, solid; $\sim 0.8 < T_g/T < 1$, semisolid; and $T_g/T \leq \sim 0.8$, liquid.

bulk, and ten bulk layers. We consider a two-component system consisting of a condensing species and a pre-existing nonvolatile species. The particle population is assumed to be monodisperse with a particle diameter of 100 nm. The total particle mass concentration, temperature, and gas-phase concentration are supplied from the GEOS-Chem simulations, and bulk diffusivities at given RH are used as described above.

τ_{eq} is calculated for the first instance (t) when the following inequality is satisfied[14]

$$\frac{|C_p(t) - C_{p\cdot eq}|}{|C_{p,0} - C_{p\cdot eq}|} < \frac{1}{e} \tag{8}$$

We simulated partitioning under the closed system in which condensation of semivolatile species depletes its gas-phase mass concentration (C_g) as its particle-phase mass concentration increases (C_p). This closed system representation best emulates the conditions in which simulated chemistry occurs within GEOS-Chem grid cells at each chemical time step. Note that we also simulated using the open system in which C_g was kept constant, and we obtained very similar spatial distributions with slightly longer τ_{eq}. Initial gas-phase mass concentrations ($C_{g,0}$) and T are supplied by GEOS-Chem and MERRA-2 ambient temperature outputs, respectively. $C_{p,0}$ and $C_{p,eq}$ refer to the initial and equilibrium mass concentrations of diffusing compounds in the particle phase, respectively. Note that τ_{eq} differs from τ_{mix}, as a homogeneously mixed bulk phase is not a necessary requirement to achieve a gas-particle partitioning equilibrium. While τ_{mix} is solely determined by bulk diffusivity and particle diameter, τ_{eq} is additionally affected by volatility and total ambient particle number concentration.[14,24,84]

τ_{eq} is calculated for the ASOA and TSOA species. Compounds with a low volatility tend to have a higher enthalpy of vaporization, ΔH_{vap} (kJ mol^{-1}), which can be described by the semiempirical parametrization[85,86]

$$\Delta H_{vap} = -5.7 \times \log_{10} C^*(300\text{ K}) + 129 \tag{9}$$

Although VOC oxidation products have been distributed into four intrinsic C^* (300 K) volatility bins from the GEOS-Chem model, the actual volatilities are ambient temperature-dependent so that the volatility of the oxidation products at a given temperature, $C^*(T)$ is calculated using the Clausius–Clapeyron relation[87]

$$C^*(T) = C^*(300\ \text{K})\exp\left(\frac{\Delta H_{\text{vap}}}{R}\left(\frac{1}{300\ \text{K}} - \frac{1}{T}\right)\right) \tag{10}$$

where R is the molar gas constant in J mol^{-1} K^{-1} and T (K) refers to the ambient temperature.

We also calculate the effective mass accommodation coefficient (α_{eff}), which is the probability of a gas molecule colliding with the surface to enter the particle phase by accounting for kinetic limitations of bulk diffusion[88]

$$\alpha_{\text{eff}} = \alpha_s \frac{1}{1 + (\alpha_s \omega C^0)/4D_b\rho_p)(r_p/5) \times 10^{-12}} \tag{11}$$

α_{eff} is dependent on the surface accommodation coefficient α_s which is assumed to be 1, mean thermal velocity ω (cm s^{-1}), volatility (μg m^{-3}) of the condensing species, bulk diffusivity D_b (cm^2 s^{-1}), and the particle density ρ_p (g cm^{-3}). α_{eff} provides an efficient way of accounting for the influence of volatility and diffusivity on the SOA partitioning.

■ RESULTS AND DISCUSSION

Global SOA Phase State Estimation. We averaged the monthly values of the glass transition temperature (T_g) scaled by the mean ambient temperature (T) for all SOA species to give annually averaged T_g/T global distributions using mean RH at the surface (1013 hPa), at 850 hPa around the boundary layer height, and at 500 hPa in the free troposphere. Note that finer temporal variabilities like diurnal cycles are not captured and actual ambient SOA phase state may also depend on local conditions;[43,89] therefore, our results should be taken as a generalized description of seasonal variations of global phase state distribution. As shown in Figure 1, for the surface level, the phase state of SOA is predicted to be mostly liquid in tropical and polar air with high RH, semisolid at the midlatitudes, and solid over arid continental lands. SOA particles in the southeastern US and Central Amazon are predicted to be liquid at the surface in agreement with particle bounce measurements indicating liquid-like behavior.[90,91] The model predicts an amorphous semisolid phase state in semiarid regions including the western US, Mexico, southern South America, sub-Saharan Africa, southern Europe, India, and Australia. This prediction is consistent with microscopic measurements which found that ambient organic particles collected in California, Mexico City, and Chile were highly viscous.[92] The model predicts that SOA particles in Midwestern US are on the lower end of the semisolid state, which is consistent with measurements at a forest site in Michigan showing that SOA particles adopt semisolid or liquid states.[89] Marine SOA are also simulated to be semisolid over midlatitude oceans even with high RH (Figure S1) as they have relatively high $T_{g,\text{org}}$ (Figure S3) with higher contributions from ASOA[64] (Figure S2). A very recent study has shown that organic components in sea spray aerosols can adopt a semisolid phase state during the peak of phytoplankton bloom, which induces the emission of high molecular weight organic and biological material,[93] while this process is not resolved in GEOS-Chem. Solid ($T_g/T > 1$) particles are predicted to be prevalent over the western US, North Africa, and Central Asia under low RH (Figure S1). Ambient samples collected from a boreal forest in Finland (60°N, 25°E), at sampling RH of 10–15%, adopt a glassy solid state in agreement with the T_g/T predictions within the same RH range as shown in Figure S4.[10] The spatial distribution of SOA phase state resembles geospatial RH patterns (Figure S1) at the surface, indicating that water uptake is a critical process in determining SOA phase state.[94]

SOA particles are predicted to increasingly adopt semisolid and solid phase states at higher altitudes, which is especially prevalent for the northern hemisphere. As we are not considering the temporal variability of clouds in the free troposphere, the associated RH variability and propensity for liquid particles are not shown in these annual averages. $T_{g,\text{org}}$ becomes higher (Figure S3) as SOA particles age upon vertical transport. Above the planetary boundary layer, semisolid particles expand off the west coast of US into the Pacific Ocean (around 30° N, 110° W) as well as off the west coast of northern Africa into the mid-Atlantic (around 20° N, 30° W) (Figure 1). Most of the continental northern hemisphere including Europe, North America, Africa, Southwest Asia, and Russia are estimated to have semisolid particles apart from Southeast Asia (around 100° E, 20° N), which has very humid conditions. While continental regions within the Arctic Circle (>66° N) are predominantly liquid near the surface due to very high RH, SOA particles in this region are mainly semisolid to solid at 850 hPa. The coastal perimeters of Greenland and Antarctica are predicted to have glassy particles governed by lower RH compared to the inland (Figures S1 and S5). In the southern hemisphere, SOA particles above Indonesia, Central Africa, and Amazonia remain liquid under moderate temperatures and high RH (Figures 1 and S1). Overall, the northern hemisphere is predicted to have SOA particles in highly viscous semisolid or glassy solid phases when transported into the free troposphere, while they adopt comparatively less viscous semisolid or liquid states in the southern hemisphere including equatorial regions of South America, Sub-Saharan Africa, and Southeast Asia due to the plasticizing effect of water under high RH (Figure S1). In summary, the majority of the globe is dominated by a liquid phase (73% of locations, based on annual average values) at the surface, a semisolid phase (70%) at 850 hPa, and a glassy solid phase (60%) at 500 hPa (Table S5). This trend agrees with the spatial distributions from a previous study using the global chemistry climate model EMAC.[38]

We conducted several sensitivity studies to evaluate the assumptions applied to our simulations. Prescribed base case O:C values used in our simulations span the range of 0.18 and 1.0 (Table S4) while ambient urban OA O:C ranges between values of 0.2 and 0.8 with diurnal variation, with areas experiencing increased SOA oxidation reaching an O:C of 1.0.[95] Measurement of O:C from OA mixtures obtained from AMS have uncertainties within ∼27% associated with the elemental ratio calculation methodology used.[96] To test the sensitivity of T_g/T on O:C, we considered a ± 50% change in O:C values, widening the range to 0.09 and 1.5, to test extreme values of O:C as well as considering multigenerational oxidation products that increase O:C.[95,97] For each SOA species, this results in a less than 0.5% change in the calculation of T_g/T, which is due to the greater role of volatility on T_g (Figure S6).[43,94] Additionally, we accounted for the formation of (E)LVOCs in the oxidation products of monoterpenes and sesquiterpenes (TSOA) species by changing the lowest volatility bin of the TSOA species from 0.1 to 1 × 10^{-4} μg m^{-3}, resulting up to a 5% change in T_g/T (Figure S6). We

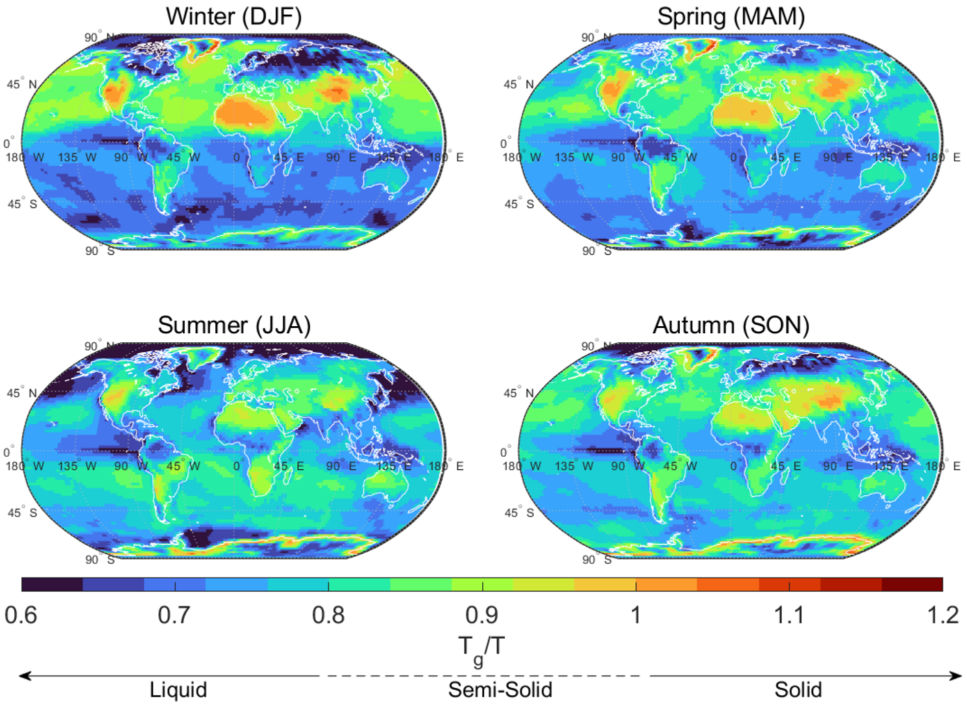

Figure 2. Predicted glass transition temperature (T_g) scaled by ambient temperature (T) for SOA (T_g/T) at the surface level in four seasons in the year 2020. T_g/T is a measure of the phase state: $T_g/T \geq 1$, solid; $\sim 0.8 < T_g/T < 1$, semisolid; and $T_g/T \leq \sim 0.8$, liquid.

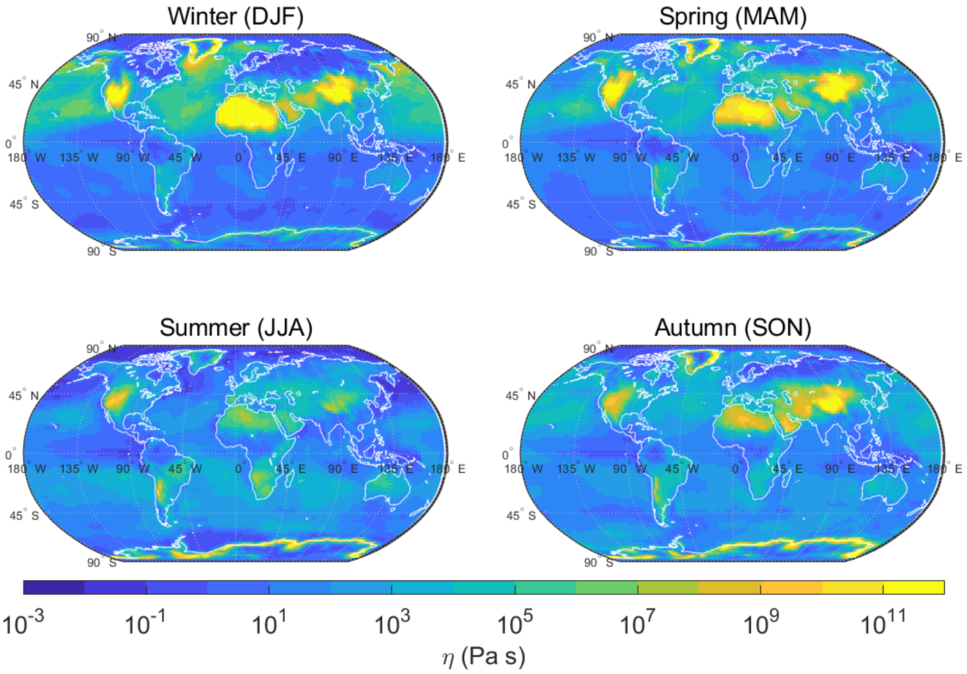

Figure 3. Predicted viscosities (η) of SOA in four seasons in 2020 at surface level (with values of $\eta > 10^{13}$ Pa s capped at 10^{13} Pa s).

tested the effects of representing the ASOA species with the semivolatile bins instead of GEOS-Chem's VBS by changing the lowest volatility bin from 1×10^{-4} to 0.1 μg m^{-3}. The resultant change in T_g/T is less than 8%, lower than the base case scenario with the most affected regions being the Western US, the Saharan Desert, and the Tibetan Plateau (Figure S6). While the assumed κ of 0.1 was for typical aged organic aerosols, we test the sensitivity of the water uptake of SOA particles by increasing or decreasing κ by 50% that would cover the range of marine or continental mean κ values.[98,99] The relative change of T_g/T is overall lower by ~5% or higher by ~10% when κ is increased or lowered by 50%, respectively, indicating that the water uptake of SOA particles and plasticizing effect by water are critical for driving the SOA phase state; thus, resolution of κ (rather than fixing its value) in a global model would improve phase state predictions in future studies. We also calculate T_g of OPOA using T_g parametrization based on only volatility (Table S7 and eq (S1)). This inclusion of OPOA results in predictions of largely similar global distributions of SOA phase state (Figure S6),

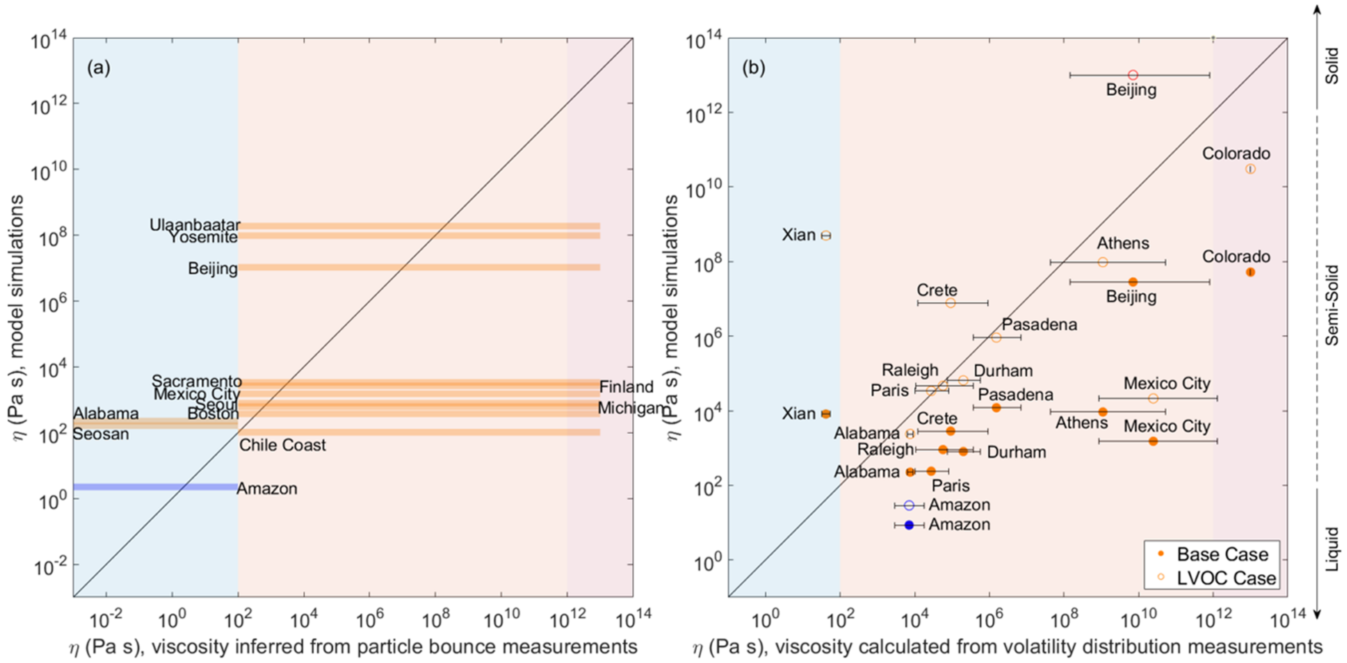

Figure 4. Comparison of predicted SOA viscosities with ambient viscosity data based on (a) particle bounce measurements (bars) and (b) volatility distribution measurements (dots). Particle viscosities calculated from measured volatility distributions at global sites compared to the viscosities predicted using GEOS-Chem's default VBS are indicated by filled markers (Base Case). Measured volatility distributions at global sites compared to the viscosity predicted in GEOS-Chem when the lowest C^* bin for all GEOS-Chem SOA species is lowered to C^* (300 K) = 10^{-4} μg m^{-3} are indicated by open markers (LVOC Case). The color code for data points indicates the SOA phase state as estimated by model simulations (blue = liquid, orange = semisolid, and red = solid). Conditions were set for 2020 at surface level (with values of $\eta > 10^{13}$ Pa s capped at 10^{13} Pa s). While the color code for the background indicates the respective phase state ranges associated with the x-axis as viscosity ($\eta < 10^2$ Pa s as liquid, $10^2 > \eta > 10^{12}$ Pa s as semisolid, and $\eta > 10^{12}$ Pa s as solid).

while there is a small decrease (<2%) in T_g/T in western US and Sahara, but for most other locations, there is overall an increase (<15%) in T_g/T (Figure S6).

Seasonal Variations of the SOA Phase State. Figure 2 shows the seasonal variations of averaged T_g/T at the surface (DJF as winter, MAM as spring, JJA as summer, and SON as autumn, as the meteorological seasons in the northern hemisphere). In fall, winter, and spring, the T_g/T values range between 0.6 and 1.1, whereas in summer, the range is shifted lower to 0.5 and 1.0 under higher temperatures. The T_g/T seasonal mean value remained constant at 0.8 throughout the year, which may be due to opposing seasonal changes in temperature and RH; for example, an increase of temperature from winter into spring is associated with a slight decrease in RH in the northern midlatitudes (Figure S7). Additionally, the fractional contribution of each SOA species to the calculated dry $T_{g,org}$ shows that during the colder months, anthropogenic SOA (ASOA) contributions are higher (Figure S8) while during the warmer months biogenic SOA (TSOA, LVOCOA, SOAIE, and SOAGX) become more dominant (Figure S9). The occurrence of semisolid and solid phase states ($T_g/T > 1$) is more frequent in the winter compared to the summer (Table S8). Northern Africa and southwest Asia are regions with a stark seasonal shifts from a semisolid/solid particle phase in the winter to a semisolid/liquid phase in the summer. In the western US, SOA particles remain semisolid and solid in all seasons due to the dry climate with small temperature variations.[43] In the Atacama Desert (20° S, 69° W) and Southern Africa, the SOA phase state is predicted to be less viscous as $T_{g,org}$ is predicted to be <270 K (Figure S3). In Antarctica with very low temperatures, the phase state is still predicted to be liquid due to very high RH.

Figure 3 shows the seasonal variation for the predicted viscosities of SOA at the surface by converting T_g/T into viscosity. Highly viscous particles with ($10^8 < \eta < 10^{12}$ Pa s) are predominantly found over the western US, northern Africa, and southwestern Asia. In a previous study over the contiguous US using the CMAQ model, SOA exists in a more viscous state ($\eta > 10^8$ Pa s) in the dry western areas of the US compared to the humid eastern US,[43] which aligns well with our predictions. Liquid and semisolid phase states are predicted in a significant portion of the continental Pacific Northwest in winter and spring, while in the summer months, the extent of the highly viscous particles stretches throughout the Pacific Northwest. We find that viscosity over central northeastern China is $\eta > 10^4$ Pa s, over the northern Tibetan plateau is $\eta > 10^8$ Pa s, and in southeastern China is $\eta < 10^4$ Pa s (Figure 3). This trend resembles geospatial pattern of RH (Figure S10) and these results are fully consistent with a very recent study, by Zhang et al.,[45] which simulated SOA phase state over China using a regional model (WRF-Chem). One difference is that we predicted semisolid particles during the summer 2020 over the southern Tibetan plateau, while Zhang et al.[45] predicted liquid particles in this location in the summer 2018 (Figure 2). This discrepancy may be attributed to a difference in simulated SOA mass concentrations, as the meteorology remains relatively consistent. It is worth mentioning that the trends in SOA mass contribution from anthropogenic sources during 2020 have been reported to differ depending on local conditions despite the widespread reduction in primary emissions during the coronavirus pandemic.[100,101] Nevertheless, the interannual

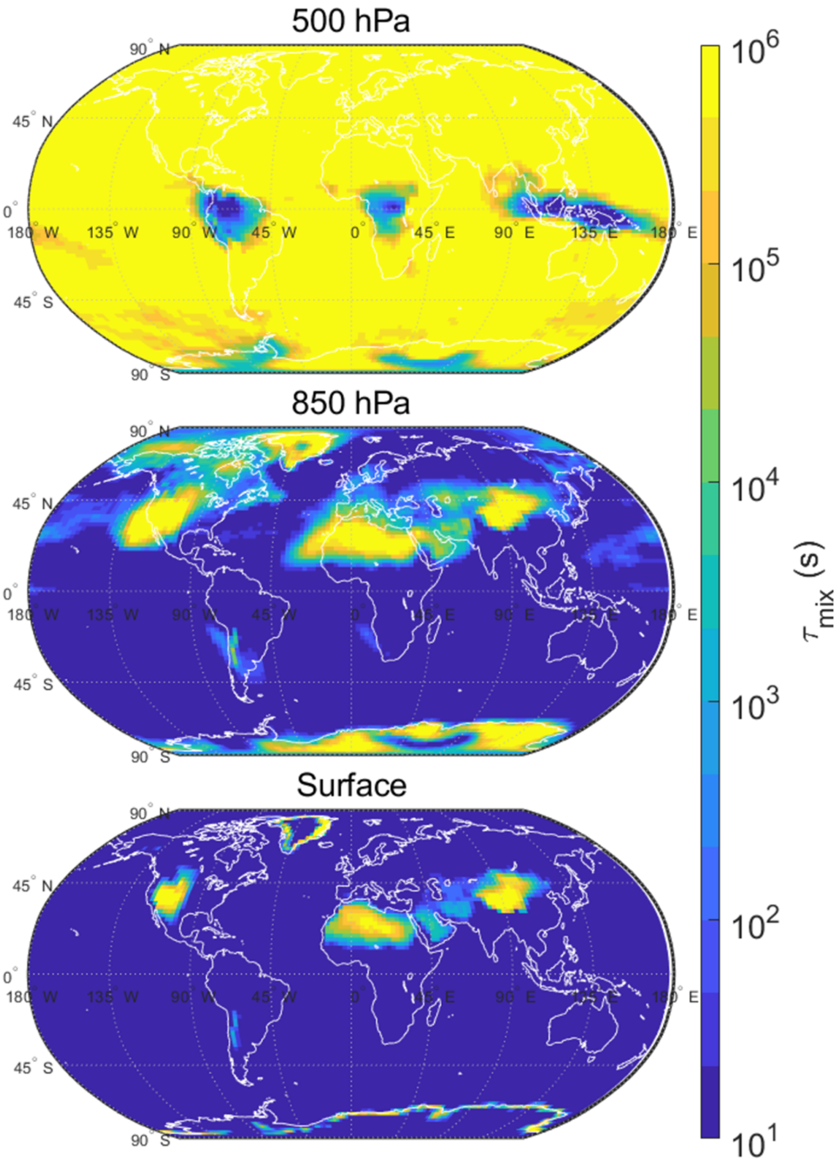

Figure 5. Predicted characteristic mixing time scales of organic molecules (τ_{mix}) in SOA particles at the surface, 850 hPa, and 500 hPa for the year 2020.

variability of the SOA phase state is not expected to be large as the model predictions of phase state presented here for 2020 agrees well with previous modeling studies using different simulation time periods.[38,43]

Model Comparison with Observations. To validate our global distributions of SOA phase state, we compare simulated SOA viscosity with viscosity inferred from particle bounce measurements (Figure 4a), which represent semiquantitative measurements by categorizing particles to be liquid-like ($\eta < 10^2$ Pa s) or semisolid or solid ($\eta > 10^2$ Pa s).[9,91] Figure 4a compiled 13 measurements, showing that the simulated viscosities are mostly consistent with particle bounce measurements, as the majority of particle bounce experiments agree with the phase state categorizations. While bounce measurements are semiquantitative measurements with large uncertainties on viscosity,[91] they are still useful for model validation. Note that the particle mixing state is not resolved in GEOS-Chem, whereas ambient SOA particles may be internally mixed with inorganic compounds, which may act as a plasticizer to reduce the viscosity. Further model development and measurements of particle viscosity and mixing state are required to address this issue in future studies.

Unfortunately, there are few direct measurements of viscosity, as these require the use of offline instruments with sufficient sample mass that is difficult with field measurements.[8] However, there are plenty of measurements of volatility distributions of ambient organic particles which can be utilized to calculate viscosity as described in detail in Li et al.[39] Using the measured volatility distributions at 11 sites as compiled by Li et al.,[39] we calculated viscosity using RH and T outputted by the MERRA-2 reanalysis product, seasonally or annually averaged in 2020 and corresponding to the months of each campaign.[39] Note that we added one more recent measurement in Xi'an, China.[102] We assumed a hygroscopicity of 0.1 to account for water uptake. The solid markers in Figure 4b show a comparison between simulated viscosity by GEOS-Chem and inferred viscosity from volatility distribution measurements. The agreement is overall satisfactory, considering the relatively coarse resolution in GEOS-Chem and uncertainty in inferred viscosity; nevertheless, GEOS-Chem

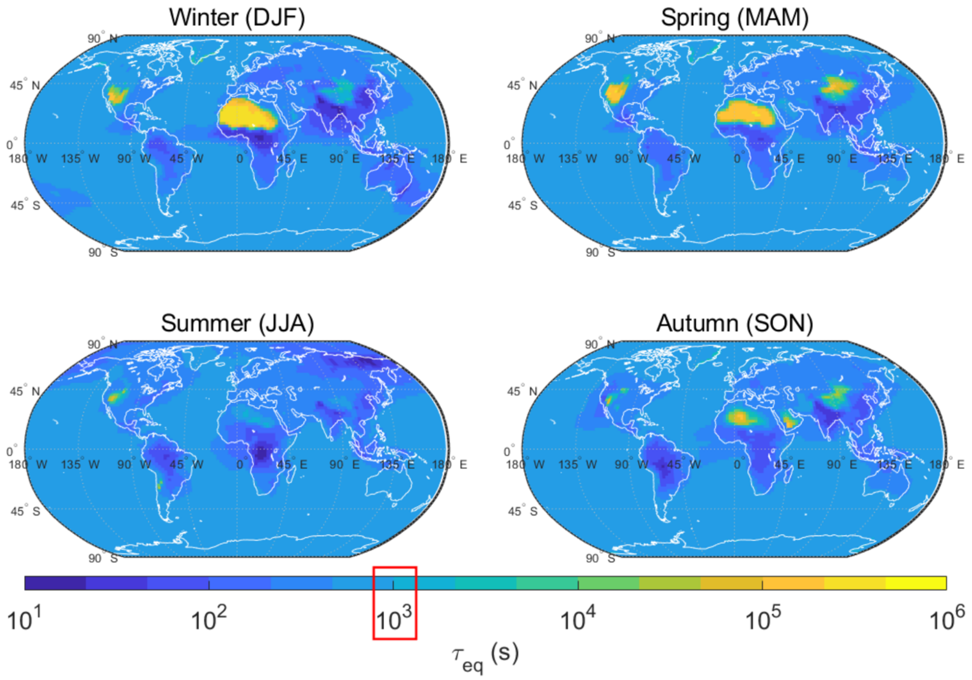

Figure 6. Seasonal variations of predicted equilibration time scales of SOA partitioning (τ_{eq}) at surface level for GEOS-Chem species TSOA in the volatility bin C^*(300 K) = 0.1 μg m^{-3}. The chemical time step of GEOS-Chem of 20 min (approximately 10^3 s) is marked by the red rectangle.

appears to systematically underestimate viscosities. This disagreement can be explained as the measured volatility distributed in a broader range including IVOCs, LVOCs, and ELVOCs (with the majority of distribution as $C^* < 10^{-3}$ μg m^{-3}) compared to the VBS used in GEOS-Chem with C^* of 0.1−100 μg m^{-3}. The missing treatment of such low-volatility products can lead to model underestimation, as LVOCs and ELVOCs would have a higher T_g. To account for this, we reduced the lowest C^* bin to C^* (300 K) = 10^{-4} μg m^{-3} in the "LVOC case", resulting in much better agreement as shown in open markers in Figure 4b. Note that the overestimation for Xi'an is further exaggerated, as oxidation products with C^* (300 K) > 100 μg m^{-3} account for a significant portion of volatility products,[102] which is not TSOA and ASOA volatility bins. Future studies on comparison with ambient measurements are warranted to further improve simulations of SOA volatility distributions and the SOA phase state in GEOS-Chem.

Characteristic Mixing Time Scales. Viscosity can be converted into bulk diffusivity using a fractional Stokes−Einstein equation as shown in Figure S11. We further calculated the characteristic mixing time scales of bulk diffusion in a single particle with a particle diameter of 100 nm (τ_{mix}) in Figure 5. τ_{mix} at the surface is shorter than 1 h over the oceans, tropics, and high altitudes, while τ_{mix} is as long as 1 day for continental regions with arid climates including Western US, northern Africa, and the Mid East. Above the boundary layer at 850 hPa, τ_{mix} becomes longer over a wider portion of the regions especially over midlatitudes. In the free troposphere at 500 hPa, τ_{mix} is very long over days (except for the tropical regions), indicating that SOA particles would not be well-mixed with concentration gradients within particles. The overall spatial and vertical distributions of τ_{mix} agree well with previous work using EMAC,[38] while here we predict shorter τ_{mix} for the majority of Eurasia and for continental areas in the southern hemisphere. τ_{mix} in the free troposphere above tropical continents has a shorter τ_{mix}, which also has been suggested by Evoy et al.[82]

Equilibration Time Scales of SOA Partitioning and Effective Mass Accommodation Coefficients. It is important to note that the quantity τ_{mix}, which describes the time scale to reach a homogeneously well-mixed particle, is not equivalent to τ_{eq}, which is the time scale to establish partitioning of semivolatile compounds between the gas and particle phases. The application of τ_{eq} is more relevant to validate the assumption of equilibrium SOA partitioning applied in current GEOS-Chem (ver. 14.1.1). τ_{eq} can be compared with the standard chemical time step of 20 min that is applied in the horizontal resolution (2 × 2.5°) of our GEOS-Chem simulations. The assumption of equilibrium SOA partitioning would not hold for locations where $\tau_{eq} > \sim 10^3$ s. Figure 6 shows seasonal variations of τ_{eq} at the surface for TSOA species with the volatility C^*(300 K) = 0.1 μg m^{-3}, partitioning to particles with a diameter of 100 nm. In summer and autumn, most of the globe has $\tau_{eq} < \sim 10^3$ s with the exception of the continental Pacific Northwest US. In winter and spring, τ_{eq} is still within 10^3 s for most continents, but it can be longer than 10^5 s (~27 h) in drylands including the Sahara, Western US, and northern China. We also simulated τ_{eq} with volatilities of C^*(300 K) of 1.0, 10, and 100 μg m^{-3} by seasons and annual averaged (Figures S12−S15). In the regions where SOA particles adopt liquid or low viscous semisolid states (over the oceans, tropical regions, etc.), τ_{eq} is shorter for compounds with high volatility as lower amounts of mass need to be transferred from the gas to the particle phase. In contrast, in the regions where SOA particles adopt highly viscous semisolid or glassy phase states (Sahara, Western US, northern China, etc.), τ_{eq} is shorter for lower volatility compounds as they condense onto particles due to their low-volatility nature; for semivolatile compounds, τ_{eq} is prolonged as re-evaporation outcompetes slower diffusion into the bulk.[14,103] We also tested the sensitivity of τ_{eq} to the particle

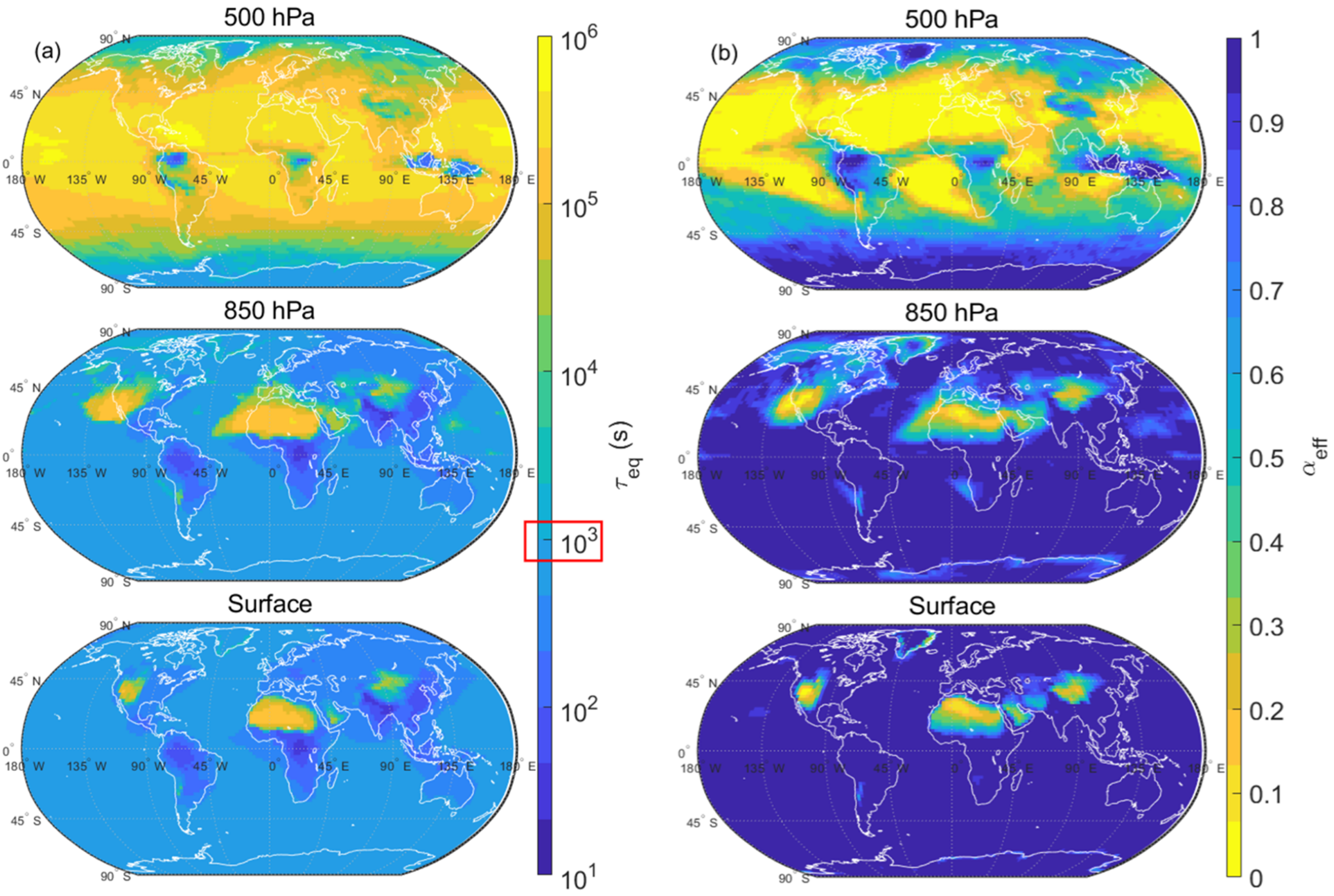

Figure 7. Global distributions of (a) equilibration time scales of SOA partitioning (τ_{eq}) and (b) effective mass accommodation coefficient (α_{eff}) at the surface level, 850 and 500 hPa for GEOS-Chem species TSOA in the volatility bin $C^*(300\ \mathrm{K}) = 0.10\ \mu\mathrm{g\ m^{-3}}$ condensing onto particles with a diameter of 100 nm, annually averaged for 2020.

size by considering a diameter of 200 nm with the same particle mass concentration (Figure S16). τ_{eq} becomes up to 1 order of magnitude longer with very similar spatial distribution as the number and surface area concentration of the particles decrease, thereby lowering the surface accommodation, requiring longer times for partitioning.[15]

Figure 7a shows the altitudinal variation in τ_{eq} for the TSOA products with $C^*(300\ \mathrm{K}) = 0.1\ \mu\mathrm{g\ m^{-3}}$ annually averaged for 2020. C^* was adjusted at higher altitude using the Clausius–Clapeyron equation. At the surface, τ_{eq} is shorter than 10^3 s in most regions but very long over the western US, northern Africa, and Western China. Then at 850 hPa, the extent of area with prolonged τ_{eq} increased, covering the majority of midlatitude continental and oceanic areas compared to the surface. In the free troposphere at 500 hPa, τ_{eq} is longer than 10^5 s for midlatitudes as particles are highly viscous under low temperatures but remain shorter at $\sim 10^3$ s in tropical regions where SOA particles are less viscous. τ_{eq} is also relatively short at $\sim 10^4$ s in polar regions as very low temperature lowers volatility of condensing species to shorten τ_{eq}.[14] Note that ambient OA mass loadings in the upper troposphere are very low (Figure S17), indicating that the condensation sink is very small also contributing to prolonged τ_{eq}.[14] Comparison between the distributions of τ_{mix} and τ_{eq} (Figures 4 and 7) reveal that at the surface, the τ_{eq} is often longer than τ_{mix}, as τ_{eq} considers mass transport from the gas to particle phase whereas τ_{mix} represents only bulk diffusion in low viscous particles. At higher altitudes, τ_{eq} is often shorter than τ_{mix}, as SOA partitioning can reach equilibrium even though there may be bulk concentration gradients in particles.

Figure 7b shows the global distribution of α_{eff} at the surface, 850 hPa, and in the free troposphere for SOA with a particle diameter of 100 nm. At the surface, α_{eff} is equal to unity for most places, indicating little kinetic limitations on mass accommodation. α_{eff} is less than 0.4 over the western US, northern Africa, and Western China, indicating that kinetic limitations of bulk diffusion would induce suppression of condensation by >60%. Above the boundary layer at 850 hPa, the regions with α_{eff} are expanded to include the western US and its coast of the Pacific Ocean, northern Africa and its coast of the Atlantic Ocean, and Northwestern China. The spatial distributions of α_{eff} at the surface and at 850 hPa are very similar to those of τ_{eq}, indicating that mass accommodation as modulated by the phase state drives the establishment of a gas-particle equilibrium. In the free troposphere at 500 hPa, α_{eff} is mostly <0.1 in the midlatitudes, indicating strong kinetic limitations to retard SOA partitioning by >90%. It is remarkable to note that α_{eff} is still high at >0.8 over tropical regions including the Amazon, central Africa, and Southeast Asia and polar regions likely due to the average high RH from frequent cloud cover (Figure S1).

Relatively short τ_{eq} and high α_{eff} at 500 hPa predicted over the Amazon rainforest suggest that SOA formation and partitioning are not restricted. This is consistent with field observations of new particle formation (NPF) events in the free troposphere and transport of these particles to lower

https://doi.org/10.1021/acsearthspacechem.4c00281
ACS Earth Space Chem. 2025, 9, 288−302

altitude by rainfall as confirmed by a modeling study.[104] The study highlights the importance of decreased volatility of organics and increased NPF efficiency at low temperatures.[105] Global NPF simulations have shown that NPF over rainforests is mostly due to organic-mediated and organic-ion-induced contributions when at high altitudes.[106] While τ_{eq} is even shorter at the surface in the Amazon, NPF was shown to be suppressed by the emission of biogenic salt particles acting as competitive particle seeds compared to nucleation events.[107] For simulating SOA growth, Zaveri et al.[19] showed the importance of the phase state and kinetic limitations in reproducing the observed evolution of particle size distribution.

The equilibrium partitioning approach can faithfully reproduce the total SOA mass but fails to accurately capture the growth of nanoparticles and aerosol size distributions.[19] Our results show that equilibrium partitioning is a good assumption for most of the globe, yet there exist regions where kinetic limitations should be considered to accurately capture dynamic aerosol behavior in the atmosphere. As α_{eff} depends on particle size, tracking the aerosol size distribution would result in an improved description of phase state effects on SOA formation and growth.

CONCLUSIONS AND IMPLICATIONS

This study presents global distributions and seasonal variations of SOA phase state, viscosity, bulk diffusivity, characteristic mixing time scale of bulk diffusion, equilibration time scale of SOA partitioning, and effective mass accommodation coefficient. While there must be large temporal variations that are masked by the seasonally and annually averaged values, we show that generally equilibrium SOA partitioning should be valid in most places at the surface, except drylands in the Sahara, Western US and northern China where SOA formation may not be substantial. In the free troposphere, kinetic limitations become more significant especially at 500 hPa as shown by long τ_{eq} and small α_{eff}. In this case, the application of instantaneous equilibrium SOA partitioning would overestimate SOA mass, and kinetically limited SOA growth would need to be considered. Capturing an accurate picture of SOA behavior and fate as it pertains to climate in modern CTMs remains a challenge. The size dependence of τ_{eq} and α_{eff} can be critical to consider the impacts of phase state on SOA formation, partitioning, and evolution of mass and size distributions of SOA. While we applied equilibrium SOA partitioning and evaluated the extent of kinetic limitations with τ_{eq} and α_{eff} in this study, we plan to implement α_{eff} to consider mass transport kinetics in GEOS-Chem to simulate SOA growth in our follow-up study. This treatment should provide better predictions of SOA mass and size distribution and, hence, improve organic aerosol budgets and aerosol effects on air quality, climate, and public health.

ASSOCIATED CONTENT

Supporting Information

The Supporting Information is available free of charge at https://pubs.acs.org/doi/10.1021/acsearthspacechem.4c00281.

> Summary of model uncertainties, the GEOS-Chem model inputs and variables, the KM-GAP model inputs and variables; sensitivity studies on the calculation the glass transition temperature scaled by ambient temperature (T_g/T); global simulations of environmental variables: temperature and relative humidity; additional global distributions of SOA phase states, equilibration time scales (τ_{eq}), and effective mass accommodation coefficients (α_{eff}) at different altitudes and seasons; and global distributions of OA mass loadings and temperature corrected effective saturation mass concentrations of terpene-derived SOA; including Tables S1−S8 and Figures S1−S19 (PDF)

AUTHOR INFORMATION

Corresponding Author

Manabu Shiraiwa − *Department of Chemistry, University of California, Irvine, California 92617, United States;* orcid.org/0000-0003-2532-5373; Email: m.shiraiwa@uci.edu

Authors

Regina Luu − *Department of Chemistry, University of California, Irvine, California 92617, United States*
Meredith Schervish − *Department of Chemistry, University of California, Irvine, California 92617, United States;* orcid.org/0009-0002-3365-9007
Nicole A. June − *Department of Atmospheric Science, Colorado State University, Fort Collins, Colorado 80521, United States;* orcid.org/0000-0002-9548-0507
Samuel E. O'Donnell − *Department of Atmospheric Science, Colorado State University, Fort Collins, Colorado 80521, United States*
Shantanu H. Jathar − *Department of Mechanical Engineering, Colorado State University, Fort Collins, Colorado 80521, United States;* orcid.org/0000-0003-4106-2358
Jeffrey R. Pierce − *Department of Atmospheric Science, Colorado State University, Fort Collins, Colorado 80521, United States;* orcid.org/0000-0002-4241-838X

Complete contact information is available at: https://pubs.acs.org/10.1021/acsearthspacechem.4c00281

Notes

The authors declare no competing financial interest.

ACKNOWLEDGMENTS

This work was funded by the U.S. National Science Foundation (AGS-2246502) and the U.S. Department of Energy (DE-SC0022139, DE-SC0021208). We thank Dr. Ying Li (Institute of Atmospheric Physics, Chinese Academy of Sciences) for the helpful discussion.

REFERENCES

(1) Andreae, M. O.; Rosenfeld, D. Aerosol−Cloud−Precipitation Interactions. Part 1. The Nature and Sources of Cloud-Active Aerosols. *Earth-Sci. Rev.* **2008**, *89* (1), 13−41.

(2) Hallquist, M.; Wenger, J. C.; Baltensperger, U.; Rudich, Y.; Simpson, D.; Claeys, M.; Dommen, J.; Donahue, N. M.; George, C.; Goldstein, A. H.; Hamilton, J. F.; Herrmann, H.; Hoffmann, T.; Iinuma, Y.; Jang, M.; Jenkin, M. E.; Jimenez, J. L.; Kiendler-Scharr, A.; Maenhaut, W.; McFiggans, G.; Mentel, T. F.; Monod, A.; Prévôt, A. S. H.; Seinfeld, J. H.; Surratt, J. D.; Szmigielski, R.; Wildt, J. The Formation, Properties and Impact of Secondary Organic Aerosol: Current and Emerging Issues. *Atmos. Chem. Phys.* **2009**, *9* (14), 5155−5236.

(3) Shrivastava, M.; Cappa, C. D.; Fan, J.; Goldstein, A. H.; Guenther, A. B.; Jimenez, J. L.; Kuang, C.; Laskin, A.; Martin, S. T.; Ng, N. L.; Petaja, T.; Pierce, J. R.; Rasch, P. J.; Roldin, P.; Seinfeld, J.

H.; Shilling, J.; Smith, J. N.; Thornton, J. A.; Volkamer, R.; Wang, J.; Worsnop, D. R.; Zaveri, R. A.; Zelenyuk, A.; Zhang, Q. Recent Advances in Understanding Secondary Organic Aerosol: Implications for Global Climate Forcing. *Rev. Geophys.* **2017**, *55* (2), 509−559.

(4) Ignatius, K.; Kristensen, T. B.; Järvinen, E.; Nichman, L.; Fuchs, C.; Gordon, H.; Herenz, P.; Hoyle, C. R.; Duplissy, J.; Garimella, S.; Dias, A.; Frege, C.; Höppel, N.; Tröstl, J.; Wagner, R.; Yan, C.; Amorim, A.; Baltensperger, U.; Curtius, J.; Donahue, N. M.; Gallagher, M. W.; Kirkby, J.; Kulmala, M.; Möhler, O.; Saathoff, H.; Schnaiter, M.; Tomé, A.; Virtanen, A.; Worsnop, D.; Stratmann, F. Heterogeneous Ice Nucleation of Viscous Secondary Organic Aerosol Produced from Ozonolysis of α-Pinene. *Atmospheric Chem. Phys.* **2016**, *16* (10), 6495−6509.

(5) Kroll, J. H.; Seinfeld, J. H. Chemistry of Secondary Organic Aerosol: Formation and Evolution of Low-Volatility Organics in the Atmosphere. *Atmos. Environ.* **2008**, *42* (16), 3593−3624.

(6) Pankow, J. F. An Absorption Model of Gas/Particle Partitioning of Organic Compounds in the Atmosphere. *Atmos. Environ.* **1994**, *28* (2), 185−188.

(7) Koop, T.; Bookhold, J.; Shiraiwa, M.; Pöschl, U. Glass Transition and Phase State of Organic Compounds: Dependency on Molecular Properties and Implications for Secondary Organic Aerosols in the Atmosphere. *Phys. Chem. Chem. Phys.* **2011**, *13* (43), 19238−19255.

(8) Reid, J. P.; Bertram, A. K.; Topping, D. O.; Laskin, A.; Martin, S. T.; Petters, M. D.; Pope, F. D.; Rovelli, G. The Viscosity of Atmospherically Relevant Organic Particles. *Nat. Commun.* **2018**, *9* (1), No. 956.

(9) Saukko, E.; Lambe, A. T.; Massoli, P.; Koop, T.; Wright, J. P.; Croasdale, D. R.; Pedernera, D. A.; Onasch, T. B.; Laaksonen, A.; Davidovits, P.; Worsnop, D. R.; Virtanen, A. Humidity-Dependent Phase State of SOA Particles from Biogenic and Anthropogenic Precursors. *Atmospheric Chem. Phys.* **2012**, *12* (16), 7517−7529.

(10) Virtanen, A.; Joutsensaari, J.; Koop, T.; Kannosto, J.; Yli-Pirilä, P.; Leskinen, J.; Mäkelä, J. M.; Holopainen, J. K.; Pöschl, U.; Kulmala, M.; Worsnop, D. R.; Laaksonen, A. An Amorphous Solid State of Biogenic Secondary Organic Aerosol Particles. *Nature* **2010**, *467* (7317), 824−827.

(11) Maclean, A. M.; Smith, N. R.; Li, Y.; Huang, Y.; Hettiyadura, A. P. S.; Crescenzo, G. V.; Shiraiwa, M.; Laskin, A.; Nizkorodov, S. A.; Bertram, A. K. Humidity-Dependent Viscosity of Secondary Organic Aerosol from Ozonolysis of β-Caryophyllene: Measurements, Predictions, and Implications. *ACS Earth Space Chem.* **2021**, *5* (2), 305−318.

(12) Petters, S. S.; Kreidenweis, S. M.; Grieshop, A. P.; Ziemann, P. J.; Petters, M. D. Temperature- and Humidity-Dependent Phase States of Secondary Organic Aerosols. *Geophys. Res. Lett.* **2019**, *46* (2), 1005−1013.

(13) Pöschl, U.; Shiraiwa, M. Multiphase Chemistry at the Atmosphere−Biosphere Interface Influencing Climate and Public Health in the Anthropocene. *Chem. Rev.* **2015**, *115* (10), 4440−4475.

(14) Li, Y.; Shiraiwa, M. Timescales of Secondary Organic Aerosols to Reach Equilibrium at Various Temperatures and Relative Humidities. *Atmospheric Chem. Phys.* **2019**, *19* (9), 5959−5971.

(15) Shiraiwa, M.; Seinfeld, J. H. Equilibration Timescale of Atmospheric Secondary Organic Aerosol Partitioning *Geophys. Res. Lett.* 2012; Vol. 39 24 DOI: 10.1029/2012GL054008.

(16) He, Y.; Akherati, A.; Nah, T.; Ng, N. L.; Garofalo, L. A.; Farmer, D. K.; Shiraiwa, M.; Zaveri, R. A.; Cappa, C. D.; Pierce, J. R.; Jathar, S. H. Particle Size Distribution Dynamics Can Help Constrain the Phase State of Secondary Organic Aerosol. *Environ. Sci. Technol.* **2021**, *55* (3), 1466−1476.

(17) Perraud, V.; Bruns, E. A.; Ezell, M. J.; Johnson, S. N.; Yu, Y.; Alexander, M. L.; Zelenyuk, A.; Imre, D.; Chang, W. L.; Dabdub, D.; Pankow, J. F.; Finlayson-Pitts, B. J. Nonequilibrium Atmospheric Secondary Organic Aerosol Formation and Growth. *Proc. Natl. Acad. Sci. U. S. A.* **2012**, *109* (8), 2836−2841.

(18) Zaveri, R. A.; Shilling, J. E.; Zelenyuk, A.; Zawadowicz, M. A.; Suski, K.; China, S.; Bell, D. M.; Veghte, D.; Laskin, A. Particle-Phase Diffusion Modulates Partitioning of Semivolatile Organic Compounds to Aged Secondary Organic Aerosol. *Environ. Sci. Technol.* **2020**, *54* (5), 2595−2605.

(19) Zaveri, R. A.; Wang, J.; Fan, J.; Zhang, Y.; Shilling, J. E.; Zelenyuk, A.; Mei, F.; Newsom, R.; Pekour, M.; Tomlinson, J.; Comstock, J. M.; Shrivastava, M.; Fortner, E.; Machado, L. A. T.; Artaxo, P.; Martin, S. T. Rapid Growth of Anthropogenic Organic Nanoparticles Greatly Alters Cloud Life Cycle in the Amazon Rainforest. *Sci. Adv.* **2022**, *8* (2), No. eabj0329.

(20) Gorkowski, K.; Preston, T. C.; Zuend, A. Relative-Humidity-Dependent Organic Aerosol Thermodynamics via an Efficient Reduced-Complexity Model. *Atmospheric Chem. Phys.* **2019**, *19* (21), 13383−13407.

(21) Loza, C. L.; Coggon, M. M.; Nguyen, T. B.; Zuend, A.; Flagan, R. C.; Seinfeld, J. H. On the Mixing and Evaporation of Secondary Organic Aerosol Components. *Environ. Sci. Technol.* **2013**, *47* (12), 6173−6180.

(22) Ye, Q.; Robinson, E. S.; Ding, X.; Ye, P.; Sullivan, R. C.; Donahue, N. M. Mixing of Secondary Organic Aerosols versus Relative Humidity. *Proc. Natl. Acad. Sci. U. S. A.* **2016**, *113* (45), 12649−12654.

(23) Ye, Q.; Upshur, M. A.; Robinson, E. S.; Geiger, F. M.; Sullivan, R. C.; Thomson, R. J.; Donahue, N. M. Following Particle-Particle Mixing in Atmospheric Secondary Organic Aerosols by Using Isotopically Labeled Terpenes. *Chem.* **2018**, *4* (2), 318−333.

(24) Schervish, M.; Shiraiwa, M. Impact of Phase State and Non-Ideal Mixing on Equilibration Timescales of Secondary Organic Aerosol Partitioning. *Atmospheric Chem. Phys.* **2023**, *23* (1), 221−233.

(25) Knopf, D. A.; Alpert, P. A. Atmospheric Ice Nucleation. *Nat. Rev. Phys.* **2023**, *5* (4), 203−217.

(26) Murray, B. J.; Wilson, T. W.; Dobbie, S.; Cui, Z.; Al-Jumur, S. M. R. K.; Möhler, O.; Schnaiter, M.; Wagner, R.; Benz, S.; Niemand, M.; Saathoff, H.; Ebert, V.; Wagner, S.; Kärcher, B. Heterogeneous Nucleation of Ice Particles on Glassy Aerosols under Cirrus Conditions. *Nat. Geosci.* **2010**, *3* (4), 233−237.

(27) Slade, J. H.; Shiraiwa, M.; Arangio, A.; Su, H.; Pöschl, U.; Wang, J.; Knopf, D. A. Cloud Droplet Activation through Oxidation of Organic Aerosol Influenced by Temperature and Particle Phase State. *Geophys. Res. Lett.* **2017**, *44* (3), 1583−1591.

(28) Zobrist, B.; Marcolli, C.; Pedernera, D. A.; Koop, T. Do Atmospheric Aerosols Form Glasses? *Atmospheric Chem. Phys.* **2008**, *8* (17), 5221−5244.

(29) Shiraiwa, M.; Ammann, M.; Koop, T.; Pöschl, U. Gas Uptake and Chemical Aging of Semisolid Organic Aerosol Particles. *Proc. Natl. Acad. Sci. U. S. A.* **2011**, *108* (27), 11003−11008.

(30) Kuwata, M.; Zorn, S. R.; Martin, S. T. Using Elemental Ratios to Predict the Density of Organic Material Composed of Carbon, Hydrogen, and Oxygen. *Environ. Sci. Technol.* **2012**, *46* (2), 787−794.

(31) Zhang, Y.; Chen, Y.; Lambe, A. T.; Olson, N. E.; Lei, Z.; Craig, R. L.; Zhang, Z.; Gold, A.; Onasch, T. B.; Jayne, J. T.; Worsnop, D. R.; Gaston, C. J.; Thornton, J. A.; Vizuete, W.; Ault, A. P.; Surratt, J. D. Effect of the Aerosol-Phase State on Secondary Organic Aerosol Formation from the Reactive Uptake of Isoprene-Derived Epoxydiols (IEPOX). *Environ. Sci. Technol. Lett.* **2018**, *5* (3), 167−174.

(32) Zhou, S.; Hwang, B. C. H.; Lakey, P. S. J.; Zuend, A.; Abbatt, J. P. D.; Shiraiwa, M. Multiphase Reactivity of Polycyclic Aromatic Hydrocarbons Is Driven by Phase Separation and Diffusion Limitations. *Proc. Natl. Acad. Sci. U. S. A.* **2019**, *116* (24), 11658−11663.

(33) Davies, J. F.; Wilson, K. R. Nanoscale Interfacial Gradients Formed by the Reactive Uptake of OH Radicals onto Viscous Aerosol Surfaces. *Chem. Sci.* **2015**, *6* (12), 7020−7027.

(34) Alpert, P. A.; Arroyo, P. C.; Dou, J.; K Krieger, U.; S Steimer, S.; Förster, J.-D.; Ditas, F.; Pöhlker, C.; Rossignol, S.; Passananti, M.; Perrier, S.; George, C.; Shiraiwa, M.; Berkemeier, T.; Watts, B.; Ammann, M. Visualizing Reaction and Diffusion in Xanthan Gum Aerosol Particles Exposed to Ozone. *Phys. Chem. Chem. Phys.* **2019**, *21* (37), 20613−20627.

(35) Mu, Q.; Shiraiwa, M.; Octaviani, M.; Ma, N.; Ding, A.; Su, H.; Lammel, G.; Pöschl, U.; Cheng, Y. Temperature Effect on Phase State

and Reactivity Controls Atmospheric Multiphase Chemistry and Transport of PAHs. *Sci. Adv.* **2018**, *4* (3), No. eaap7314.

(36) DeRieux, W.-S. W.; Li, Y.; Lin, P.; Laskin, J.; Laskin, A.; Bertram, A. K.; Nizkorodov, S. A.; Shiraiwa, M. Predicting the Glass Transition Temperature and Viscosity of Secondary Organic Material Using Molecular Composition. *Atmospheric Chem. Phys.* **2018**, *18* (9), 6331−6351.

(37) Evoy, E.; Kamal, S.; Patey, G. N.; Martin, S. T.; Bertram, A. K. Unified Description of Diffusion Coefficients from Small to Large Molecules in Organic−Water Mixtures. *J. Phys. Chem. A* **2020**, *124* (11), 2301−2308.

(38) Shiraiwa, M.; Li, Y.; Tsimpidi, A. P.; Karydis, V. A.; Berkemeier, T.; Pandis, S. N.; Lelieveld, J.; Koop, T.; Pöschl, U. Global Distribution of Particle Phase State in Atmospheric Secondary Organic Aerosols. *Nat. Commun.* **2017**, *8* (1), No. 15002.

(39) Li, Y.; Day, D. A.; Stark, H.; Jimenez, J. L.; Shiraiwa, M. Predictions of the Glass Transition Temperature and Viscosity of Organic Aerosols from Volatility Distributions. *Atmospheric Chem. Phys.* **2020**, *20* (13), 8103−8122.

(40) Donahue, N. M.; Epstein, S. A.; Pandis, S. N.; Robinson, A. L. A Two-Dimensional Volatility Basis Set: 1. Organic-Aerosol Mixing Thermodynamics. *Atmospheric Chem. Phys.* **2011**, *11* (7), 3303−3318.

(41) Rasool, Q. Z.; Shrivastava, M.; Liu, Y.; Gaudet, B.; Zhao, B. Modeling the Impact of the Organic Aerosol Phase State on Multiphase OH Reactive Uptake Kinetics and the Resultant Heterogeneous Oxidation Timescale of Organic Aerosol in the Amazon Rainforest. *ACS Earth Space Chem.* **2023**, 7 (5), 1009−1024.

(42) Zhang, Z.; Li, Y.; Ran, H.; An, J.; Qu, Y.; Zhou, W.; Xu, W.; Hu, W.; Xie, H.; Wang, Z.; Sun, Y.; Shiraiwa, M. *Phase State and Viscosity of Secondary Organic Aerosols over China Simulated by WRF-Chem.*; preprint; Aerosols/Atmospheric Modelling and Data Analysis/Troposphere/Physics (physical properties and processes), 2023. DOI: 10.5194/egusphere-2023-1444.

(43) Li, Y.; Carlton, A. G.; Shiraiwa, M. Diurnal and Seasonal Variations in the Phase State of Secondary Organic Aerosol Material over the Contiguous US Simulated in CMAQ. *ACS Earth Space Chem.* **2021**, *5* (8), 1971−1982.

(44) Schmedding, R.; Rasool, Q. Z.; Zhang, Y.; Pye, H. O. T.; Zhang, H.; Chen, Y.; Surratt, J. D.; Lopez-Hilfiker, F. D.; Thornton, J. A.; Goldstein, A. H.; Vizuete, W. Predicting Secondary Organic Aerosol Phase State and Viscosity and Its Effect on Multiphase Chemistry in a Regional-Scale Air Quality Model. *Atmospheric Chem. Phys.* **2020**, *20* (13), 8201−8225.

(45) Zhang, Z.; Li, Y.; Ran, H.; An, J.; Qu, Y.; Zhou, W.; Xu, W.; Hu, W.; Xie, H.; Wang, Z.; Sun, Y.; Shiraiwa, M. Simulated Phase State and Viscosity of Secondary Organic Aerosols over China. *Atmospheric Chem. Phys.* **2024**, *24* (8), 4809−4826.

(46) Lin, H.; Emmons, L. K.; Lundgren, E. W.; Yang, L. H.; Feng, X.; Dang, R.; Zhai, S.; Tang, Y.; Kelp, M. M.; Colombi, N. K.; Eastham, S. D.; Fritz, T. M.; Jacob, D. J. Intercomparison of GEOS-Chem and CAM-Chem Tropospheric Oxidant Chemistry within the Community Earth System Model Version 2 (CESM2). *Atmospheric Chem. Phys.* **2024**, *24* (15), 8607−8624.

(47) Fu, Y.; Pang, Q.; Zhuo Ga, Suo. Lang.; Wu, P.; Wang, Y.; Mao, M.; Yuan, Z.; Xu, X.; Liu, K.; Wang, X.; Li, D.; Zhang, Y. Modeling Atmospheric Microplastic Cycle by GEOS-Chem: An Optimized Estimation by a Global Dataset Suggests Likely 50 Times Lower Ocean Emissions. *One Earth* **2023**, *6* (6), 705−714.

(48) Community, T. I. G.-C. U. *Geoschem/GCClassic: GCClassic 14.4.1*, 2024.

(49) Gelaro, R.; McCarty, W.; Suárez, M. J.; Todling, R.; Molod, A.; Takacs, L.; Randles, C. A.; Darmenov, A.; Bosilovich, M. G.; Reichle, R.; Wargan, K.; Coy, L.; Cullather, R.; Draper, C.; Akella, S.; Buchard, V.; Conaty, A.; Silva, A. M. da.; Gu, W.; Kim, G.-K.; Koster, R.; Lucchesi, R.; Merkova, D.; Nielsen, J. E.; Partyka, G.; Pawson, S.; Putman, W.; Rienecker, M.; Schubert, S. D.; Sienkiewicz, M.; Zhao, B. *The Modern-Era Retrospective Analysis for Research and Applications*, Version 2 (MERRA-2)2017.

(50) Lin, H.; Jacob, D. J.; Lundgren, E. W.; Sulprizio, M. P.; Keller, C. A.; Fritz, T. M.; Eastham, S. D.; Emmons, L. K.; Campbell, P. C.; Baker, B.; Saylor, R. D.; Montuoro, R. Harmonized Emissions Component (HEMCO) 3.0 as a Versatile Emissions Component for Atmospheric Models: Application in the GEOS-Chem, NASA GEOS, WRF-GC, CESM2, NOAA GEFS-Aerosol, and NOAA UFS Models. *Geosci. Model Dev.* **2021**, *14* (9), 5487−5506.

(51) Hoesly, R. M.; Smith, S. J.; Feng, L.; Klimont, Z.; Janssens-Maenhout, G.; Pitkanen, T.; Seibert, J. J.; Vu, L.; Andres, R. J.; Bolt, R. M.; Bond, T. C.; Dawidowski, L.; Kholod, N.; Kurokawa, J.; Li, M.; Liu, L.; Lu, Z.; Moura, M. C. P.; O'Rourke, P. R.; Zhang, Q. Historical (1750−2014) Anthropogenic Emissions of Reactive Gases and Aerosols from the Community Emissions Data System (CEDS). *Geosci. Model Dev.* **2018**, *11* (1), 369−408.

(52) Weng, H.; Lin, J.; Martin, R.; Millet, D. B.; Jaeglé, L.; Ridley, D.; Keller, C.; Li, C.; Du, M.; Meng, J. Global High-Resolution Emissions of Soil NOx, Sea Salt Aerosols, and Biogenic Volatile Organic Compounds. *Sci. Data* **2020**, *7*, 148.

(53) Guenther, A. B.; Jiang, X.; Heald, C. L.; Sakulyanontvittaya, T.; Duhl, T.; Emmons, L. K.; Wang, X. The Model of Emissions of Gases and Aerosols from Nature Version 2.1 (MEGAN2.1): An Extended and Updated Framework for Modeling Biogenic Emissions. *Geosci. Model Dev.* **2012**, *5* (6), 1471−1492.

(54) Marais, E. A.; Jacob, D. J.; Jimenez, J. L.; Campuzano-Jost, P.; Day, D. A.; Hu, W.; Krechmer, J.; Zhu, L.; Kim, P. S.; Miller, C. C.; Fisher, J. A.; Travis, K.; Yu, K.; Hanisco, T. F.; Wolfe, G. M.; Arkinson, H. L.; Pye, H. O. T.; Froyd, K. D.; Liao, J.; McNeill, V. F. Aqueous-Phase Mechanism for Secondary Organic Aerosol Formation from Isoprene: Application to the Southeast United States and Co-Benefit of SO_2 Emission Controls. *Atmospheric Chem. Phys.* **2016**, *16* (3), 1603−1618.

(55) Fisher, J. A.; Jacob, D. J.; Travis, K. R.; Kim, P. S.; Marais, E. A.; Chan Miller, C.; Yu, K.; Zhu, L.; Yantosca, R. M.; Sulprizio, M. P.; Mao, J.; Wennberg, P. O.; Crounse, J. D.; Teng, A. P.; Nguyen, T. B.; St Clair, J. M.; Cohen, R. C.; Romer, P.; Nault, B. A.; Wooldridge, P. J.; Jimenez, J. L.; Campuzano-Jost, P.; Day, D. A.; Hu, W.; Shepson, P. B.; Xiong, F.; Blake, D. R.; Goldstein, A. H.; Misztal, P. K.; Hanisco, T. F.; Wolfe, G. M.; Ryerson, T. B.; Wisthaler, A.; Mikoviny, T. Organic Nitrate Chemistry and Its Implications for Nitrogen Budgets in an Isoprene- and Monoterpene-Rich Atmosphere: Constraints from Aircraft (SEAC^{4}RS) and Ground-Based (SOAS) Observations in the Southeast US. *Atmospheric Chem. Phys.* **2016**, *16* (9), 5969−5991.

(56) Bianchi, F.; Kurtén, T.; Riva, M.; Mohr, C.; Rissanen, M. P.; Roldin, P.; Berndt, T.; Crounse, J. D.; Wennberg, P. O.; Mentel, T. F.; Wildt, J.; Junninen, H.; Jokinen, T.; Kulmala, M.; Worsnop, D. R.; Thornton, J. A.; Donahue, N.; Kjaergaard, H. G.; Ehn, M. Highly Oxygenated Organic Molecules (HOM) from Gas-Phase Autoxidation Involving Peroxy Radicals: A Key Contributor to Atmospheric Aerosol. *Chem. Rev.* **2019**, *119* (6), 3472−3509.

(57) Tröstl, J.; Chuang, W. K.; Gordon, H.; Heinritzi, M.; Yan, C.; Molteni, U.; Ahlm, L.; Frege, C.; Bianchi, F.; Wagner, R.; Simon, M.; Lehtipalo, K.; Williamson, C.; Craven, J. S.; Duplissy, J.; Adamov, A.; Almeida, J.; Bernhammer, A.-K.; Breitenlechner, M.; Brilke, S.; Dias, A.; Ehrhart, S.; Flagan, R. C.; Franchin, A.; Fuchs, C.; Guida, R.; Gysel, M.; Hansel, A.; Hoyle, C. R.; Jokinen, T.; Junninen, H.; Kangasluoma, J.; Keskinen, H.; Kim, J.; Krapf, M.; Kürten, A.; Laaksonen, A.; Lawler, M.; Leiminger, M.; Mathot, S.; Möhler, O.; Nieminen, T.; Onnela, A.; Petäjä, T.; Piel, F. M.; Miettinen, P.; Rissanen, M. P.; Rondo, L.; Sarnela, N.; Schobesberger, S.; Sengupta, K.; Sipilä, M.; Smith, J. N.; Steiner, G.; Tomè, A.; Virtanen, A.; Wagner, A. C.; Weingartner, E.; Wimmer, D.; Winkler, P. M.; Ye, P.; Carslaw, K. S.; Curtius, J.; Dommen, J.; Kirkby, J.; Kulmala, M.; Riipinen, I.; Worsnop, D. R.; Donahue, N. M.; Baltensperger, U. The Role of Low-Volatility Organic Compounds in Initial Particle Growth in the Atmosphere. *Nature* **2016**, *533* (7604), 527−531.

(58) Xu, R.; Thornton, J. A.; Lee, B. H.; Zhang, Y.; Jaeglé, L.; Lopez-Hilfiker, F. D.; Rantala, P.; Petäjä, T. Global Simulations of Monoterpene-Derived Peroxy Radical Fates and the Distributions of

Highly Oxygenated Organic Molecules (HOMs) and Accretion Products. *Atmospheric Chem. Phys.* **2022**, *22* (8), 5477−5494.

(59) Pye, H. O. T.; Chan, A. W. H.; Barkley, M. P.; Seinfeld, J. H. Global Modeling of Organic Aerosol: The Importance of Reactive Nitrogen (NO_x and NO_3). *Atmospheric Chem. Phys.* **2010**, *10* (22), 11261−11276.

(60) Hu, W.; Zhou, H.; Chen, W.; Ye, Y.; Pan, T.; Wang, Y.; Song, W.; Zhang, H.; Deng, W.; Zhu, M.; Wang, C.; Wu, C.; Ye, C.; Wang, Z.; Yuan, B.; Huang, S.; Shao, M.; Peng, Z.; Day, Douglas. A.; Campuzano-Jost, P.; Lambe, A. T.; Worsnop, D. R.; Jimenez, J. L.; Wang, X. Oxidation Flow Reactor Results in a Chinese Megacity Emphasize the Important Contribution of S/IVOCs to Ambient SOA Formation. *Environ. Sci. Technol.* **2022**, *56* (11), 6880−6893.

(61) Miao, R.; Chen, Q.; Shrivastava, M.; Chen, Y.; Zhang, L.; Hu, J.; Zheng, Y.; Liao, K. Process-Based and Observation-Constrained SOA Simulations in China: The Role of Semivolatile and Intermediate-Volatility Organic Compounds and OH Levels. *Atmospheric Chem. Phys.* **2021**, *21* (21), 16183−16201.

(62) Ma, P. K.; Zhao, Y.; Robinson, A. L.; Worton, D. R.; Goldstein, A. H.; Ortega, A. M.; Jimenez, J. L.; Zotter, P.; Prévôt, A. S. H.; Szidat, S.; Hayes, P. L. Evaluating the Impact of New Observational Constraints on P-S/IVOC Emissions, Multi-Generation Oxidation, and Chamber Wall Losses on SOA Modeling for Los Angeles, CA. *Atmospheric Chem. Phys.* **2017**, *17* (15), 9237−9259.

(63) Pai, S. J.; Heald, C. L.; Pierce, J. R.; Farina, S. C.; Marais, E. A.; Jimenez, J. L.; Campuzano-Jost, P.; Nault, B. A.; Middlebrook, A. M.; Coe, H.; Shilling, J. E.; Bahreini, R.; Dingle, J. H.; Vu, K. An Evaluation of Global Organic Aerosol Schemes Using Airborne Observations. *Atmospheric Chem. Phys.* **2020**, *20* (5), 2637−2665.

(64) Pye, H. O. T.; Seinfeld, J. H. A Global Perspective on Aerosol from Low-Volatility Organic Compounds. *Atmospheric Chem. Phys.* **2010**, *10* (9), 4377−4401.

(65) Brewer, J. F.; Jacob, D. J.; Jathar, S. H.; He, Y.; Akherati, A.; Zhai, S.; Jo, D. S.; Hodzic, A.; Nault, B. A.; Campuzano-Jost, P.; Jimenez, J. L.; Park, R. J.; Oak, Y. J.; Liao, H. A Scheme for Representing Aromatic Secondary Organic Aerosols in Chemical Transport Models: Application to Source Attribution of Organic Aerosols Over South Korea During the KORUS-AQ Campaign. *J. Geophys. Res. Atmospheres* **2023**, *128* (8), No. e2022JD037257.

(66) Murphy, B. N.; Donahue, N. M.; Robinson, A. L.; Pandis, S. N. A Naming Convention for Atmospheric Organic Aerosol. *Atmospheric Chem. Phys.* **2014**, *14* (11), 5825−5839.

(67) Grieshop, A. P.; Logue, J. M.; Donahue, N. M.; Robinson, A. L. Laboratory Investigation of Photochemical Oxidation of Organic Aerosol from Wood Fires 1: Measurement and Simulation of Organic Aerosol Evolution. *Atmospheric Chem. Phys.* **2009**, *9* (4), 1263−1277.

(68) Jathar, S. H.; Sharma, N.; Galang, A.; Vanderheyden, C.; Takhar, M.; Chan, A. W. H.; Pierce, J. R.; Volckens, J. Measuring and Modeling the Primary Organic Aerosol Volatility from a Modern Non-Road Diesel Engine. *Atmos. Environ.* **2020**, *223*, No. 117221.

(69) Sinha, A.; George, I.; Holder, A.; Preston, W.; Hays, M.; P Grieshop, A. Development of Volatility Distributions for Organic Matter in Biomass Burning Emissions. *Environ. Sci. Atmospheres* **2023**, *3* (1), 11−23.

(70) Lane, T. E.; Donahue, N. M.; Pandis, S. N. Simulating Secondary Organic Aerosol Formation Using the Volatility Basis-Set Approach in a Chemical Transport Model. *Atmos. Environ.* **2008**, *42* (32), 7439−7451.

(71) Geos-Chem/GeosCore/Carbon_mod.F90, 2024 https://github.com/geoschem/geos-chem/blob/20e2402baf56c682cc04af74adb139efdb6ca000/GeosCore/carbon_mod.F90.

(72) Wang, M.; Chen, D.; Xiao, M.; Ye, Q.; Stolzenburg, D.; Hofbauer, V.; Ye, P.; Vogel, A. L.; Mauldin, R. L. I.; Amorim, A.; Baccarini, A.; Baumgartner, B.; Brilke, S.; Dada, L.; Dias, A.; Duplissy, J.; Finkenzeller, H.; Garmash, O.; He, X.-C.; Hoyle, C. R.; Kim, C.; Kvashnin, A.; Lehtipalo, K.; Fischer, L.; Molteni, U.; Petäjä, T.; Pospisilova, V.; Quéléver, L. L. J.; Rissanen, M.; Simon, M.; Tauber, C.; Tomé, A.; Wagner, A. C.; Weitz, L.; Volkamer, R.; Winkler, P. M.; Kirkby, J.; Worsnop, D. R.; Kulmala, M.; Baltensperger, U.; Dommen, J.; El-Haddad, I.; Donahue, N. M. Photo-Oxidation of Aromatic Hydrocarbons Produces Low-Volatility Organic Compounds. *Environ. Sci. Technol.* **2020**, *54* (13), 7911−7921.

(73) Chen, B.; Mirrielees, J. A.; Chen, Y.; Onasch, T. B.; Zhang, Z.; Gold, A.; Surratt, J. D.; Zhang, Y.; Brooks, S. D. Glass Transition Temperatures of Organic Mixtures from Isoprene Epoxydiol-Derived Secondary Organic Aerosol. *J. Phys. Chem. A* **2023**, *127* (18), 4125−4136.

(74) Shiraiwa, M.; Berkemeier, T.; Schilling-Fahnestock, K. A.; Seinfeld, J. H.; Pöschl, U. Molecular Corridors and Kinetic Regimes in the Multiphase Chemical Evolution of Secondary Organic Aerosol. *Atmospheric Chem. Phys.* **2014**, *14* (16), 8323−8341.

(75) Petters, M. D.; Kreidenweis, S. M. A Single Parameter Representation of Hygroscopic Growth and Cloud Condensation Nucleus Activity. *Atmospheric Chem. Phys.* **2007**, *7* (8), 1961−1971.

(76) Lambe, A. T.; Onasch, T. B.; Massoli, P.; Croasdale, D. R.; Wright, J. P.; Ahern, A. T.; Williams, L. R.; Worsnop, D. R.; Brune, W. H.; Davidovits, P. Laboratory Studies of the Chemical Composition and Cloud Condensation Nuclei (CCN) Activity of Secondary Organic Aerosol (SOA) and Oxidized Primary Organic Aerosol (OPOA). *Atmospheric Chem. Phys.* **2011**, *11* (17), 8913−8928.

(77) Cross, E. S.; Slowik, J. G.; Davidovits, P.; Allan, J. D.; Worsnop, D. R.; Jayne, J. T.; Lewis †, D. K.; Canagaratna, M.; Onasch, T. B. Laboratory and Ambient Particle Density Determinations Using Light Scattering in Conjunction with Aerosol Mass Spectrometry. *Aerosol Sci. Technol.* **2007**, *41* (4), 343−359.

(78) You, Y.; Smith, M. L.; Song, M.; Martin, S. T.; Bertram, A. K. Liquid−Liquid Phase Separation in Atmospherically Relevant Particles Consisting of Organic Species and Inorganic Salts. *Int. Rev. Phys. Chem.* **2014**, *33* (1), 43−77.

(79) Richards, D. S.; Trobaugh, K. L.; Hajek-Herrera, J.; Price, C. L.; Sheldon, C. S.; Davies, J. F.; Davis, R. D. Ion−Molecule Interactions Enable Unexpected Phase Transitions in Organic-Inorganic Aerosol. *Sci. Adv.* **2020**, *6* (47), No. eabb5643.

(80) Tumminello, P. R.; Niles, R.; Valdez, V.; Madawala, C. K.; Gamage, D. K.; Kimble, K. A.; Leibensperger, R. J. I.; Huang, C.; Kaluarachchi, C.; Dinasquet, J.; Malfatti, F.; Lee, C.; Deane, G. B.; Stokes, M. D.; Stone, E.; Tivanski, A.; Prather, K. A.; Boor, B. E.; Slade, J. H. Size-Dependent Nascent Sea Spray Aerosol Bounce Fractions and Estimated Viscosity: The Role of Divalent Cation Enrichment, Surface Tension, and the Kelvin Effect. *Environ. Sci. Technol.* **2024**, *58* (44), 19666−19678.

(81) Angell, C. A. Entropy and Fragility in Supercooling Liquids. *J. Res. Natl. Inst. Stand. Technol.* **1997**, *102* (2), 171−185.

(82) Evoy, E.; Maclean, A. M.; Rovelli, G.; Li, Y.; Tsimpidi, A. P.; Karydis, V. A.; Kamal, S.; Lelieveld, J.; Shiraiwa, M.; Reid, J. P.; Bertram, A. K. Predictions of Diffusion Rates of Large Organic Molecules in Secondary Organic Aerosols Using the Stokes−Einstein and Fractional Stokes−Einstein Relations. *Atmospheric Chem. Phys.* **2019**, *19* (15), 10073−10085.

(83) Seinfeld, J. H.; Pandis, S. N. *Atmospheric Chemistry and Physics: From Air Pollution to Climate Change*, 3rd ed.; Wiley, 2016.

(84) Shiraiwa, M.; Pfrang, C.; Koop, T.; Pöschl, U. Kinetic Multi-Layer Model of Gas-Particle Interactions in Aerosols and Clouds (KM-GAP): Linking Condensation, Evaporation and Chemical Reactions of Organics, Oxidants and Water. *Atmospheric Chem. Phys.* **2012**, *12* (5), 2777−2794.

(85) Stolzenburg, D.; Fischer, L.; Vogel, A. L.; Heinritzi, M.; Schervish, M.; Simon, M.; Wagner, A. C.; Dada, L.; Ahonen, L. R.; Amorim, A.; Baccarini, A.; Bauer, P. S.; Baumgartner, B.; Bergen, A.; Bianchi, F.; Breitenlechner, M.; Brilke, S.; Buenrostro Mazon, S.; Chen, D.; Dias, A.; Draper, D. C.; Duplissy, J.; El Haddad, I.; Finkenzeller, H.; Frege, C.; Fuchs, C.; Garmash, O.; Gordon, H.; He, X.; Helm, J.; Hofbauer, V.; Hoyle, C. R.; Kim, C.; Kirkby, J.; Kontkanen, J.; Kürten, A.; Lampilahti, J.; Lawler, M.; Lehtipalo, K.; Leiminger, M.; Mai, H.; Mathot, S.; Mentler, B.; Molteni, U.; Nie, W.; Nieminen, T.; Nowak, J. B.; Ojdanic, A.; Onnela, A.; Passananti, M.; Petäjä, T.; Quéléver, L. L. J.; Rissanen, M. P.; Sarnela, N.; Schallhart,

S.; Tauber, C.; Tomé, A.; Wagner, R.; Wang, M.; Weitz, L.; Wimmer, D.; Xiao, M.; Yan, C.; Ye, P.; Zha, Q.; Baltensperger, U.; Curtius, J.; Dommen, J.; Flagan, R. C.; Kulmala, M.; Smith, J. N.; Worsnop, D. R.; Hansel, A.; Donahue, N. M.; Winkler, P. M. Rapid Growth of Organic Aerosol Nanoparticles over a Wide Tropospheric Temperature Range. *Proc. Natl. Acad. Sci. U. S. A.* **2018**, *115* (37), 9122−9127.

(86) Stolzenburg, D.; Wang, M.; Schervish, M.; Donahue, N. M. Tutorial: Dynamic Organic Growth Modeling with a Volatility Basis Set. *J. Aerosol Sci.* **2022**, *166*, No. 106063.

(87) Epstein, S. A.; Riipinen, I.; Donahue, N. M. A Semiempirical Correlation between Enthalpy of Vaporization and Saturation Concentration for Organic Aerosol. *Environ. Sci. Technol.* **2010**, *44* (2), 743−748.

(88) Shiraiwa, M.; Pöschl, U. Mass Accommodation and Gas−Particle Partitioning in Secondary Organic Aerosols: Dependence on Diffusivity, Volatility, Particle-Phase Reactions, and Penetration Depth. *Atmospheric Chem. Phys.* **2021**, *21* (3), 1565−1580.

(89) Slade, J. H.; Ault, A. P.; Bui, A. T.; Ditto, J. C.; Lei, Z.; Bondy, A. L.; Olson, N. E.; Cook, R. D.; Desrochers, S. J.; Harvey, R. M.; Erickson, M. H.; Wallace, H. W.; Alvarez, S. L.; Flynn, J. H.; Boor, B. E.; Petrucci, G. A.; Gentner, D. R.; Griffin, R. J.; Shepson, P. B. Bouncier Particles at Night: Biogenic Secondary Organic Aerosol Chemistry and Sulfate Drive Diel Variations in the Aerosol Phase in a Mixed Forest. *Environ. Sci. Technol.* **2019**, *53* (9), 4977−4987.

(90) Bateman, A. P.; Gong, Z.; Liu, P.; Sato, B.; Cirino, G.; Zhang, Y.; Artaxo, P.; Bertram, A. K.; Manzi, A. O.; Rizzo, L. V.; Souza, R. A. F.; Zaveri, R. A.; Martin, S. T. Sub-Micrometre Particulate Matter Is Primarily in Liquid Form over Amazon Rainforest. *Nat. Geosci.* **2016**, *9* (1), 34−37.

(91) Pajunoja, A.; Hu, W.; Leong, Y. J.; Taylor, N. F.; Miettinen, P.; Palm, B. B.; Mikkonen, S.; Collins, D. R.; Jimenez, J. L.; Virtanen, A. Phase State of Ambient Aerosol Linked with Water Uptake and Chemical Aging in the Southeastern US. *Atmospheric Chem. Phys.* **2016**, *16* (17), 11163−11176.

(92) O'Brien, R. E.; Neu, A.; Epstein, S. A.; MacMillan, A. C.; Wang, B.; Kelly, S. T.; Nizkorodov, S. A.; Laskin, A.; Moffet, R. C.; Gilles, M. K. Physical Properties of Ambient and Laboratory-Generated Secondary Organic Aerosol. *Geophys. Res. Lett.* **2014**, *41* (12), 4347−4353.

(93) Tumminello, P. R.; James, R. C.; Kruse, S.; Kawasaki, A.; Cooper, A.; Guadalupe-Diaz, I.; Zepeda, K. L.; Crocker, D. R.; Mayer, K. J.; Sauer, J. S.; Lee, C.; Prather, K. A.; Slade, J. H. Evolution of Sea Spray Aerosol Particle Phase State Across a Phytoplankton Bloom. *ACS Earth Space Chem.* **2021**, *5* (11), 2995−3007.

(94) Rasool, Q. Z.; Shrivastava, M.; Octaviani, M.; Zhao, B.; Gaudet, B.; Liu, Y. Modeling Volatility-Based Aerosol Phase State Predictions in the Amazon Rainforest. *ACS Earth Space Chem.* **2021**, *5* (10), 2910−2924.

(95) Aiken, A. C.; DeCarlo, P. F.; Kroll, J. H.; Worsnop, D. R.; Huffman, J. A.; Docherty, K. S.; Ulbrich, I. M.; Mohr, C.; Kimmel, J. R.; Sueper, D.; Sun, Y.; Zhang, Q.; Trimborn, A.; Northway, M.; Ziemann, P. J.; Canagaratna, M. R.; Onasch, T. B.; Alfarra, M. R.; Prevot, A. S. H.; Dommen, J.; Duplissy, J.; Metzger, A.; Baltensperger, U.; Jimenez, J. L. O/C and OM/OC Ratios of Primary, Secondary, and Ambient Organic Aerosols with High-Resolution Time-of-Flight Aerosol Mass Spectrometry. *Environ. Sci. Technol.* **2008**, *42* (12), 4478−4485.

(96) Canagaratna, M. R.; Jimenez, J. L.; Kroll, J. H.; Chen, Q.; Kessler, S. H.; Massoli, P.; Hildebrandt Ruiz, L.; Fortner, E.; Williams, L. R.; Wilson, K. R.; Surratt, J. D.; Donahue, N. M.; Jayne, J. T.; Worsnop, D. R. Elemental Ratio Measurements of Organic Compounds Using Aerosol Mass Spectrometry: Characterization, Improved Calibration, and Implications. *Atmospheric Chem. Phys.* **2015**, *15* (1), 253−272.

(97) Lin, G.; Sillman, S.; Penner, J. E.; Ito, A. Global Modeling of SOA: The Use of Different Mechanisms for Aqueous-Phase Formation. *Atmospheric Chem. Phys.* **2014**, *14* (11), 5451−5475.

(98) Cerully, K. M.; Bougiatioti, A.; Hite, J. R. J.; Guo, H.; Xu, L.; Ng, N. L.; Weber, R.; Nenes, A. On the Link between Hygroscopicity, Volatility, and Oxidation State of Ambient and Water-Soluble Aerosols in the Southeastern United States. *Atmospheric Chem. Phys.* **2015**, *15* (15), 8679−8694.

(99) Pringle, K. J.; Tost, H.; Pozzer, A.; Pöschl, U.; Lelieveld, J. Global Distribution of the Effective Aerosol Hygroscopicity Parameter for CCN Activation. *Atmospheric Chem. Phys.* **2010**, *10* (12), 5241−5255.

(100) Zhong, H.; Huang, R.-J.; Chang, Y.; Duan, J.; Lin, C.; Chen, Y. Enhanced Formation of Secondary Organic Aerosol from Photochemical Oxidation during the COVID-19 Lockdown in a Background Site in Northwest China. *Sci. Total Environ.* **2021**, *778*, No. 144947.

(101) Ciarelli, G.; Jiang, J.; Haddad, I. E.; Bigi, A.; Aksoyoglu, S.; H Prévôt, A. S.; Marinoni, A.; Shen, J.; Yan, C.; Bianchi, F. Modeling the Effect of Reduced Traffic Due to COVID-19 Measures on Air Quality Using a Chemical Transport Model: Impacts on the Po Valley and the Swiss Plateau Regions. *Environ. Sci. Atmospheres* **2021**, *1* (5), 228−240.

(102) Shang, Y.; Li, L.; Sun, T.; Kong, X.; Wang, S.; Hallquist, M. Characterization and Seasonal Variation of PM2.5 Composition in Xi'an, Northwest China: Oxygenated and Nitrogenous Organic Aerosol. *ACS Earth Space Chem.* **2024**, *8* (7), 1370−1384.

(103) Schervish, M.; Donahue, N. M.; Shiraiwa, M. Effects of Volatility, Viscosity, and Non-Ideality on Particle−Particle Mixing Timescales of Secondary Organic Aerosols. *Aerosol Sci. Technol.* **2024**, *58* (4), 411−426.

(104) Wang, J.; Krejci, R.; Giangrande, S.; Kuang, C.; Barbosa, H. M. J.; Brito, J.; Carbone, S.; Chi, X.; Comstock, J.; Ditas, F.; Lavric, J.; Manninen, H. E.; Mei, F.; Moran-Zuloaga, D.; Pöhlker, C.; Pöhlker, M. L.; Saturno, J.; Schmid, B.; Souza, R. A. F.; Springston, S. R.; Tomlinson, J. M.; Toto, T.; Walter, D.; Wimmer, D.; Smith, J. N.; Kulmala, M.; Machado, L. A. T.; Artaxo, P.; Andreae, M. O.; Petäjä, T.; Martin, S. T. Amazon Boundary Layer Aerosol Concentration Sustained by Vertical Transport during Rainfall. *Nature* **2016**, *539* (7629), 416−419.

(105) Zhao, B.; Shrivastava, M.; Donahue, N. M.; Gordon, H.; Schervish, M.; Shilling, J. E.; Zaveri, R. A.; Wang, J.; Andreae, M. O.; Zhao, C.; Gaudet, B.; Liu, Y.; Fan, J.; Fast, J. D. High Concentration of Ultrafine Particles in the Amazon Free Troposphere Produced by Organic New Particle Formation. *Proc. Natl. Acad. Sci. U. S. A.* **2020**, *117* (41), 25344−25351.

(106) Zhao, B.; Donahue, N. M.; Zhang, K.; Mao, L.; Shrivastava, M.; Ma, P.-L.; Shen, J.; Wang, S.; Sun, J.; Gordon, H.; Tang, S.; Fast, J.; Wang, M.; Gao, Y.; Yan, C.; Singh, B.; Li, Z.; Huang, L.; Lou, S.; Lin, G.; Wang, H.; Jiang, J.; Ding, A.; Nie, W.; Qi, X.; Chi, X.; Wang, L. Global Variability in Atmospheric New Particle Formation Mechanisms. *Nature* **2024**, *631* (8019), 98−105.

(107) Pöhlker, C.; Wiedemann, K. T.; Sinha, B.; Shiraiwa, M.; Gunthe, S. S.; Smith, M.; Su, H.; Artaxo, P.; Chen, Q.; Cheng, Y.; Elbert, W.; Gilles, M. K.; Kilcoyne, A. L. D.; Moffet, R. C.; Weigand, M.; Martin, S. T.; Pöschl, U.; Andreae, M. O. Biogenic Potassium Salt Particles as Seeds for Secondary Organic Aerosol in the Amazon. *Science* **2012**, *337* (6098), 1075−1078.